Learning Camera-specific Semantic Knowledge for Surveillance Traffic Analysis

by

Yanzi Jin
B.A., Dalian University of Technology

THESIS

Submitted in partial fulfillment of the requirements
for the degree of Doctor of Philosophy in Computer Science
in the Graduate College of the
University of Illinois at Chicago, 2019

Chicago, Illinois

Defense Committee:
Jakob Eriksson, Chair and Advisor
Xinhua Zhang
Brian Ziebart
Jie Yang, MSCS Department
Ahmet Enis Cetin, ECE Department

Dedicated to my parents and sister, for their unconditional love and support.

ACKNOWLEDGMENT

I would like thank my advisor Dr. Jakob Eriksson throughout these years for his support and instructions. He is very visionary about this interesting and challenging project. I admire his academic attitude and time he spent to learn together with students. I appreciate the time that we went through the code line by line for a hidden bug or hours of discussion of algorithm details. Thanks to his generous freedom and support, I got comprehensive training and became independent and mature in research.

Also, I would like express appreciation to my committee members, for their advice and inspiration. I took their classes and learned preliminary knowledge of different research areas. Specifically I want to thank Dr. Xinhua Zhang, whose rigorous attitude toward research and passion of teaching greatly inspired me. And Dr. Jie Yang's rich experience gave me helpful guidance of many technical questions.

In addition, I want to thank my parents and sister. My father teaches me to be strong and tough; my mother supports me for all my big decisions; my sister takes care of my parents when I am far away. Finally, special thanks to Sihong Xie, for his accompany and encouragement along this tough journey.

YJ

CONTRIBUTIONS OF AUTHORS

Chapter 2 represents a published manuscripts with complete citation, where I am the first author. My advisor Jakob Eriksson contributes to the writing of it. Other parts of this thesis consist of my own unpublished experiments.

TABLE OF CONTENTS

TABLE OF CONTENTS (Continued)

CHAPTER **PAGE**

LIST OF TABLES

LIST OF FIGURES

LIST OF FIGURES (Continued)

FIGURE **PAGE**

LIST OF FIGURES (Continued)

FIGURE **PAGE**

SUMMARY

One to two page summary of the entire work. Like a long abstract.

CHAPTER 1

INTRODUCTION

1.1 Surveillance monitoring via computer vision

Surveillance tasks are an essential source of decision making for monitoring and management purpose. A private commercial shopping mall may need the statistics of customer visit count and average shopping time to analyze sale performance; surveillance record may provide evidence to the police and help to solve criminal cases; people civil engineering department may need the data of traffic flow and speed for better traffic signal design. Hand-held counting device or written record at the interested location were widely used to keep track of people. For vehicles on the road, sizeable physical equipment was mainly used, such as pressure tubes laid across the pavement, magnetic loops under the pavement (1; 2). These equipment are usually hard to set up and maintain; therefore are generally labor expensive.

With the progress of the hardware, the cost of cameras has been significantly reduced. Compared with the traditional heavy and inefficient equipment, they are more lightweight and easier to set up. Due to the low cost and full coverage of the surveillance area, surveillance cameras are prevalently installed all across the city and run continuously. The following abundant video data demand efficient indexing and information extraction for surveillance tasks, involving interdisciplinary research such database and video/image processing.

1.2 Computer vision on surveillance data

With the progress in artificial intelligence and higher demand in its application, computer vision is becoming one of its hottest sub-domains. Computer vision enables computers to perform tasks that human is good at, such as visual detection and tracking. With the superior advantage of computational speed, these tasks could be applied in large scale.

When the fundamental theory of this field has become rather mature, researchers gradually shift their attention to more specific tasks and data. For example, pedestrian detection (3) and face recognition (4), gesture recognition (5) has become individual topics due to their huge application potential and high demand. On the other hand, surveillance videos have also drawn much attention because of the various practical challenges and the huge impact of applications. Researchers are studying the computer vision problems specific to surveillance videos, such as anomaly detection (6), tracking (7) and counting (8).

The surveillance videos have a few unique features:

- they are recorded ceaselessly, therefore, in large quantities;
- they are usually of low-resolution qualities due to the transmission and storage limits;
- they have a special composition (pedestrian and vehicle) and the objects in the view move in a regular motion pattern.
- depending on the location, the video may contain a large number of objects with highly complex interactions.

Therefore, the complexity of the videos and the high-performance requirement raise challenges for robust surveillance systems. Ideally, they are expected to perform the task with one-time setup and the minimal amount of human effort, with high accuracy and high speed.

1.3 Practical visual surveillance

While people in both civil engineering and computer vision are working toward the same goal — building the real-world visual surveillance systems, there is still a big gap between the state-of-the-art research and the practice use. Researchers in academia need an in-depth study of a specific problem; therefore, they usually make simplified assumptions to isolate the problem and ignore the impact of other factors. However, the real-world application runs in a complex environment and deals with noisy data. Data cleaning and processing speed have to be taken into account. For example, researchers care more about the novelty and performance of the solution and assume the computation resources are unlimited. In this case, even though some algorithms outperform human, they are too slow to process a massive amount of data. Besides, academic problems usually have a standard benchmark with well-processed data, so that people could spend the minimal amount of time on evaluation, with a uniformly acknowledged standard. However, those data might be too small and ideal compared with the real-world data, and the evaluation metric may not be comprehensive for those complex and noisy data for different tasks.

After some failed trails of computer vision algorithms on data from the local department of transportation, it turns out that noisy data is one major obstacle for processing real-world data. Besides, minimal human input and real-time processing speed is the prerequisite for

large scale application. On the other hand, there lacks a standard benchmark and dataset for the researchers in the field to study the visual surveillance problems and solve the bottleneck problem.

In this thesis, we try to address the aforementioned problems neglected in visual surveillance field and narrow the gap between the computer vision research and large scale application. Specifically, we are building an end-to-end pipeline for transportation video analysis, minimizing human input and maximizing the throughput. We aim to solve the problems in vehicle tracking and counting that are critical to the performance, such as automatic tracking initialization/termination, noise elimination. On top of that, we try to further improve the algorithm performance by learning semantic knowledge in an unsupervised manner, taking into account that the regular vehicle motion pattern from a static camera could be informative for analytic tasks. Through comprehensive experiment and case studies, we show that proper initialization and termination improves the performance of the general automatic tracking framework with any tracking algorithm; and the semantic knowledge brings more benefits to multiple visual surveillance tasks. As a by-product of our experiment, we annotate and release a large dataset for the community (9), aiming to attract and help more researchers to work on such problems.

CHAPTER 2

FULLY AUTOMATIC VEHICLE TRACKER

2.1 Introduction

Vehicle tracking has important applications in traffic engineering. Over time, a number of vehicle counting methods have been developed, including specialized hand-held counting boards with buttons to push, pressure tubes laid across the pavement, magnetic loops under the pavement (1; 2), video-based lane occupancy detectors, and more. Overall, the most powerful techniques rely on manual input and tend to be extremely labor intensive, whereas the mostly automatic techniques lack in accuracy and descriptiveness. In principle, computer vision provides the most scalable and economical alternative. Ideally, a fully automatic computer vision-based tracker follows each vehicle as it enters, traverses and exits the scene. However, current tracking algorithms such as (10; 11; 12; 13) all require initialization as input, leading to semi-automatic tracking systems. To avoid manual input, these trackers rely on background subtraction and/or object detectors for initialization. Here, the primary challenge is robustness to variations in illumination condition, viewpoint, and video quality. Background subtraction model could fail with illumination change, while detectors are not appropriate for detecting a vehicle in the distance, or in a grainy low-resolution video, as our experiments demonstrate. Additionally, the low throughput of most trackers prevents widely deployed surveillance appli-

cations, as VOT 2016 challenge reports that none of the top-ranked trackers run in real-time for even a single tracked object.

We propose a fully automatic algorithm for vehicle tracking that runs faster than real-time. With a sensor fusion approach, we combine background segmentation, object detection, and optical flow into a single, robust vehicle tracking system via Kalman filtering. Initialization uses the same three sources, to automatically identify moving objects in the scene. Finally, when an object exits the scene, its movements are analyzed to filter out unlikely object trajectories. To evaluate our algorithm as well as prior work, we create a hand-annotated dataset, consisting of 11 diverse, 5-minute videos collected from existing traffic surveillance cameras. For each frame, the location and extent of each moving object is provided, which enables accurate, quantitative evaluation.

We compare the proposed algorithm against multiple state-of-the-art trackers, which rely on human input for initialization. On this dataset, we report considerably better performance than the state of the art with manual initialization, and substantial accuracy improvement when using our new automatic initialization method. Moreover, we demonstrate throughput 4× faster than real time and over 5× improvement compared to 5 out of 7 several baseline trackers, up to 47×.

2.2 Preliminary

The problem of vehicle tracking in existing traffic surveillance video presents some unique computer vision challenges, including scale changes, video quality (exposure control, automatic white balance and compression), weather conditions, illumination changes, variations in per-

spective, and occlusion. Current work in object detection (14; 15; 16; 17), tracking (10; 12; 11) and background subtraction (18; 19) can deal with a subset of these conditions, but so far a generic system has been elusive. Below, we first introduce the underlying methods used in our system, then describe our vehicle tracking framework in detail.

2.2.1 Background subtraction

Background subtraction generates a binary foreground mask given a sequence of frames. Connected areas in the foreground mask can be treated as moving objects, although this technique can be error prone. We use ViBe (18), for its balance of speed, robustness and accuracy. However, other methods could be substituted with acceptable results in many cases.

Figure 1 summarizes four common failure cases of the background subtraction with foreground bounding boxes on the original frame on the left and the foreground on the right. Automatic exposure (Figure 1a) is performed by the camera during recording, whereas illumination variation (Figure 1b) is due to external light sources, such as the sun and vehicle headlights. Both automatic exposure and illumination variation cause rapid and widespread changes in pixel values, which most background subtraction methods struggle with. Occlusion (Figure 1c) creates a single connected foreground area out of two or more moving objects, or sometimes multiple foreground areas for a single moving object, breaking any assumption of a one-to-one mapping between foreground areas and moving object. Ghosting (Figure 1d) usually happens when a foreground object remains stationary for a long time, during which time it is gradually assimilated into the background model. When the object begins to move, what

appears from behind the object is inaccurately marked as foreground, until the background model has had time to adjust.

In summary, background subtraction provides the ability to capture small movements without manual setup beforehand. However, it is error-prone and must be compensated by other methods to create a robust vehicle tracking system.

2.2.2 Object detection

Object detectors (16; 17) work on individual frames, scanning the image for areas that appear similar to offline training samples. Compared to background subtraction, object detection method tends to be more robust to illumination change and occlusion. However, the cost of object detection is remarkable, as it often involves an exhaustive search throughout the image, both in location and object size. Cascaded classifiers partially address this by discarding background regions (16). More recently, deep neural networks (17; 20) have emerged as a promising approach to object detection. We use a state-of-the-art detector called faster-RCNN (20). Running on a high-end graphics processing unit (GPU), the time required for detection on one image drops from 2 seconds (16) to 198 ms on the PASCAL 2007 dataset, making the real-time detection in video feasible. However, like other detectors, faster-RCNN still has missing and false detections. In our measurements, it has a missing rate in excess of 65% and 86% on high- and low-resolution videos, respectively. Thus, given the high miss rate, especially on poor quality images, object detection alone will not suffice for a robust vehicle tracking system.

(a) Camera auto-exposure.

(b) Illumination change.

(c) Occlusion. Note also the shadow, due to illumination change.

(d) Ghosting. Vehicles stopped at red light have become part of the background model.

Figure 1: Common background subtraction failure cases. Pixel values change for many reasons other than motion.

2.2.3 Optical flow

Optical flow is an estimate of the movement of pixels between two images: in our case, two consecutive video frames. Optical flow provides a low-level description of motion in images and can offer useful evidence for tracking applications. Estimating optical flow is a research area in its own right, but we use the seminal Lucas-Kanade algorithm (21) in our system, as it runs fast on GPUs, and provides useful results while making minimal assumptions about the underlying scene and image. Figure 2 illustrates two optical flow problems that may affect tracking accuracy. The left column shows the direction and magnitude of the optical flow vectors, while the right column is the color code visualization of the optical flow results, with the color wheel at bottom right corner of Figure 2b indicating the corresponding direction. Figure 2a illustrates the so-called aperture problem, where the center of the truck has no reported optical flow, due to its large and uniformly colored surface. Figure 2b illustrates the "turbulent", error-prone flow that occurs where objects traveling in opposite directions meet.

Thus, while *accurate* optical flow estimates offer valuable information about movement in the scene, it is neither complete (due to the aperture problem), nor free of severe estimation errors, in particular near occlusion boundaries.

2.3 Heuristic tracker by Kalman Filter

Figure 3 describes the workflow of our automatic tracking application. We first apply background subtraction and object detector on each frame. This generates two sets of candidate boxes, which are used to initialize and update trackers. Each tracker is represented by an individual Kalman filter (22). Optical flow is also computed. Any flow that matches a tracked

(a) Aperture problem.

(b) Occlusion "turbulence".

Figure 2: Common problems in optical flow estimation.

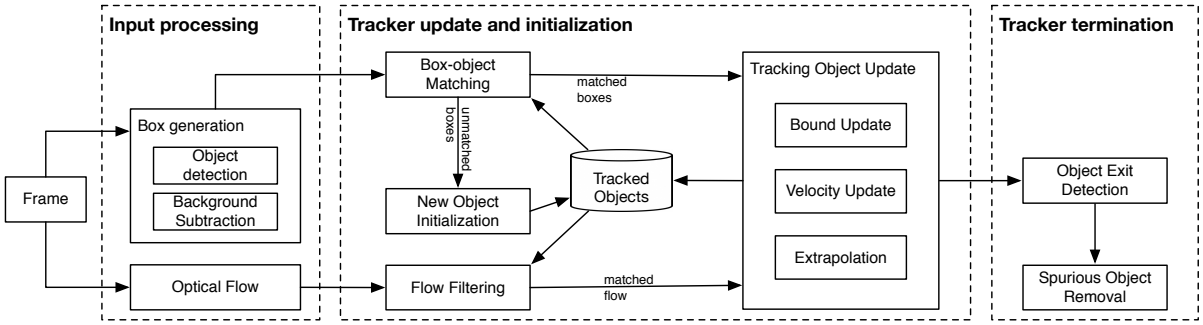

Figure 3: Overview of proposed system. Separate Kalman filter state is initialized, maintained and terminated for each tracked object. The state is updated based on matching input from background subtraction, object detection and optical flow.

object both by location and velocity, is used for tracker update. Tracking is terminated based on object location, velocity and time; short-lived or otherwise spurious objects are filtered out.

2.3.1 Model definition

We use Kalman filter to smooth out the noises in the observed measurements by the aforementioned components and more importantly, to integrate the strengths and compensate the weakness of each component. The *prediction* by its linear model is *corrected* with measurements observed over time, therefore the generated estimation is much smoother despite the noises in measurement input. To model the state change, a discrete-time controlled process is modeled as linear stochastic difference equation (23), state at time k is a linear combination of its previous state $\mathbf{x_{t-1}}$ at time $t-1$ and the process noise $\mathbf{w}_{t-1}$:

$$\mathbf{x}_k = A\mathbf{x}_{t-1} + \mathbf{w}_{t-1}, \tag{2.1}$$

where A is the state transition model. In our case, A models how object move on the frame along time, presumably satisfies constant acceleration movement. There is also measurement $\mathbf{z} \in \mathbb{R}^m$ formulated as

$$\mathbf{z}_t = H\mathbf{x}_t + \mathbf{v}_t. \tag{2.2}$$

Here H is the measure model, which observation to correct prediction from previous step. $\mathbf{w}_t$ in Equation 2.1 and $\mathbf{v}_t$ in Equation 2.2 are process and measurement noise respectively. They

are assumed independent of each other and zero-mean Gaussian, with Q and R as process noise covariance and measurement noise covariance, respectively.

$$\begin{aligned} p(\mathbf{w}) &\sim \mathcal{N}(0, Q) \\ p(\mathbf{v}) &\sim \mathcal{N}(0, R) \end{aligned} \tag{2.3}$$

The recursive process of Kalman filter contains two steps: time update (prediction) and measurement update (correction). Both steps are applied at time k, indicated by subscripts below. For such a continuous system, we define a time unit dt, which is the time interval we perform an update, in our case, the time between two consecutive frames. Each variable has its own value at a certain time step t, indicated by the subscript. The prediction is performed as follows:

$$\begin{aligned} \hat{\mathbf{x}}_t^- &= A\hat{\mathbf{x}}_{t-1} \\ P_t^- &= AP_{t-1}A^T + Q \end{aligned} \tag{2.4}$$

Here $\hat{\mathbf{x}}_{t-1}$ and $\hat{\mathbf{x}}_t^-$ are internal states before and after prediction at time t. P_{t-1} and P_t^- are prior and post error covariances, and Q is the process noise covariance. In our case, we define the internal state a 10-dimensional vector:

$$\mathbf{x} = [x, y, w, h, x', y', w', h', x'', y''],$$

corresponding to the object's top left location (x, y), size (w, h), as well as the velocity (x', y'), rate of growth (w', h') and acceleration (x'', y''), respectively. The dynamic model A is de-

fined based on the physics equation of displacement with velocity and acceleration. With the assumption that the object has constant acceleration within dt, we have:

$$\begin{aligned} x_t &= x_{t-1} + x'_{t-1} \cdot dt + \tfrac{1}{2} \cdot x''_{t-1} \cdot dt^2 \\ y_t &= y_{t-1} + y'_{t-1} \cdot dt + \tfrac{1}{2} \cdot y''_{t-1} \cdot dt^2 \\ x'_t &= x'_{t-1} + x''_{t-1} \cdot dt \\ y'_t &= y'_{t-1} + y''_{t-1} \cdot dt. \end{aligned} \tag{2.5}$$

For width and height, we instead assume constant growth rate within dt, thus

$$\begin{aligned} w_t &= w_{t-1} + w'_{t-1} \cdot dt \\ h_t &= h_{t-1} + h'_{t-1} \cdot dt \end{aligned} \tag{2.6}$$

After prediction, the estimated state $\hat{\mathbf{x}}_t^-$ is corrected by an observed measurement $\mathbf{z}$ at each time step by the steps below:

$$\begin{aligned} K_t &= P_t^- H^T (H P_t^- H^T + R)^{-1} \\ \hat{\mathbf{x}}_t &= \hat{\mathbf{x}}_t^- + K_t(\mathbf{z}_t - H\hat{\mathbf{x}}_t^-) \\ P_t &= (I - K_t H) P_t^- \end{aligned} \tag{2.7}$$

In our case, we have a 10-dimensional measurement vector:

$$\mathbf{z} = [x^{bg}, y^{bg}, w^{bg}, h^{bg}, x^{det}, y^{det}, w^{det}, h^{det}, v_x, v_y],$$

which represents the top left coordinates (x, y), width (w), height (h), reported by background subtraction bg and detector det, separately, as well as the velocity (v_x, v_y) reported by optical flow estimation. The measurement model H is a 10-by-10 matrix of zeros except for ones at $(0,0)$, $(1,1)$, $(2,2)$, $(3,3)$, $(0,4)$, $(1,5)$, $(2,6)$, $(3,7)$, $(4,8)$, $(5,9)$, signifying that the background and detector boxes directly measure x, y, w, and h, and that optical flow directly measures x' and y'. In other words, there are no direct measurements of w', h', x'' or y'' since they are not observable. R is the measurement noise covariance, indicating the noisiness of measurement. By manipulating the measurement noise covariance R, we compute a Kalman gain K_t, indicating the weight of the measurement to update the corresponding prediction.

2.3.2 Measurement acquisition

None of our input measurements: background subtraction, object detection and optical flow, correspond directly to a single tracked object. Instead, they generate boxes and flow indications for an entire frame. To produce input to an individual tracked object's filter, we first compute a matching of input data to tracked objects, then apply the matched boxes and flow to the corresponding object's Kalman filter state.

Background subtraction and object detection: Both background subtraction and object detection generate bounding boxes $\{x, y, w, h\}$. We only take those consistent with tracker's current state as the measurement. For each Kalman filter, the best matching box as measurement maximizes the total overlap between the predicted bounds of internal filter, and the bounds of the measured boxes. Boxes must overlap with the predicted state in order to be considered a match. Any remaining boxes are used to initialize new tracked objects.

Optical flow: Optical flow reports velocity on a pixel-by-pixel basis, with many erroneous flow vectors due to the aperture and turbulence problems described earlier. To produce a velocity measurement from the optical flow field for a single object, we first denoise the flow field by forward-backward error thresholding, as described in (24). We then filter the flow by location, velocity magnitude and direction. In particular, we only consider flow vectors that originate from the location of the object in the previous frame, follow the similar direction (within in 45°) of the previous state – to reduce the effect of turbulence problem, and only keep those vectors that fall within twice the error covariance (available in P, diagonal entries corresponding to the object velocity in $\hat{\mathbf{x}}$), using the simplifying assumption that flow errors follow a normal distribution. Finally we use the mean of the remaining flow vectors on horizontal and vertical direction, respectively, as the optical flow measurement for the object.

2.3.3 Model update

The measurements above are directly plugged into Equation 2.7, however, are of different quality, and oftentimes some of the measurements are missing entirely. For example, the invalid foreground is generated when occlusion happens; detector misses a small-sized object, or aperture problem gives zero movement of object. We address these problems by varying the measurement noise covariance accordingly, which in turn causes the Kalman filter to choose a gain K that maximizes the quality of the internal state. Recall in Equation 2.7, a large measurement covariance Q would result in a smaller K, therefore the measurement weights less in correction. When a measurement is missing, we use the value already in $\hat{\mathbf{x}}$ as a proxy, and set the covariance to ∞. Consequently, once none of the three measurements is available, the

tracker merely relies on the internal prediction, which we call *extrapolation*. The tracker could still generate tracking results by the internal linear model during extrapolation. The other two cases in Figure 3 are when at least one bounding box is available (bound update) or only optical flow is obtained (velocity update).

We also apply error gating to the background subtraction and object detection measurements. For example, foreground bounding box that is well overlapped with tracked objects (more than 30% overlap) has a higher confidence than those with other bounding boxes around. Similarly, optical flow have a lower confidence with zero value on both directions, since we have no idea whether the object is still or the aperture problem happens. In addition, as described in §2.2, the three measurement types naturally have different error covariances. Although detector has a higher missing rate, the recall is also high. Therefore, measurement from detector has a smaller noise covariance value than those from background model.

2.4 Fully automatic initialization and termination

2.4.1 Object entry and exit

Currently available datasets usually have tracked objects in the center of the first frame, however, we have initialization more challenging when objects enter the scene in a variety of ways: approach from a distance, enter from the image boundary, appear from behind an occluding object — moving or stationary, and become visible due to changes in lighting or background conditions. Termination has similar challenges — vehicles may disappear temporarily behind obstructions or due to changing conditions, they may linger near the edge of the screen, exit the scene while behind a moving vehicle, or disappear slowly into the distance. It is usually

natural to terminate tracking when sequence ends or object leaves the scene in short sequences, whereas in practice, it is hard to distinguish between exiting and temporal occlusion when the object is not visible in long-time videos.

As automatic initialization and termination are missing in the majority of current tracking literature, the generally accepted methods either heuristically manually label an entry/exit area beforehand, under the assumption that objects always enter or exit within a certain area, or rely on fully manual initialization. The first method is too simplistic for general purpose vehicle tracking, and the second is impractical under constrained expense/time budget for large-scale use.

In the only available literature that explicitly addresses the effect of tracker initialization (25), the author concludes that slight temporal and spatial variation would result in performance difference. However, unlike the currently available dataset, vehicles frequently encounter significant scale change while leaving or entering the scene in the traffic surveillance videos available to us. This presents a unique problem for initialization, as early initialization would result in a small, poor-quality image, and late initialization results in missing of information due to the short trajectory. Thus, striking the right balance between tracking performance and lifetime is the key to automatic tracker initialization.

2.4.2 Our method

Our system initializes new trackers based on unmatched boxes from background subtraction and object detection. This supports the challenging cases described above, but can result in many spurious trackers due to the noisy nature of both background subtraction and optical

flow. We use a two-pronged approach to limit such spurious results. First, initialization is limited to objects larger than 10×10 pixels. This reduces the number of trackers in flight, without significant negative effect: cars that could reasonably be captured tend to be larger than that in our videos, except when approaching from or driving toward the vanishing point. Second, trackers are terminated when the object leaves the frame, after no direct observations (boxes or optical flow) has been made for 50 frames, in other words, in *extrapolation* mode. Any object would have such 50 frames before exit. However, upon termination, tracked objects are validated based on the number of observations and distance traveled. Spurious noise tends to be stationary and short-lived, whereas vehicles typically follow a continuous and long-lived path through the scene. To adapt to the variety of videos and objects, distance threshold is dynamically computed by object size and video resolution. One good consequence of such scheme is that many early initialized noises are quickly discarded, since usually there is no consistent measurement available for them, while those tiny objects discarded as noises are soon available for future initialization, with better quality. Therefore, real small objects are able to be initialized at the earliest point and survive with a complete trajectory.

Algorithm 1 to 3gives the pseudo code for our method. Since it is uses heuristic criteria for initialization and termination, we call it the heuristic tracker.

2.5 Evaluation

2.5.1 Tracker configuration

To better evaluate how each component contributes to the tracker in videos under various conditions, we use three different configurations of our tracking system, based on the inputs

Algorithm 1 Heuristic tracker.

for each frame t **do**
  Obtain foreground boxes $\mathbf{R}_{bg} = \{\mathbf{r}_{bg}\}$.
  Obtain detection boxes $\mathbf{R}_{det} = \{\mathbf{r}_{det}\}$.
  for each i th object O_i at $\mathbf{r}_{t-1}(i)$, $(i = 1, \ldots, N_t)$ **do**
    Find the most matched boxes $\mathbf{r}_{bg}(i)$ and $\mathbf{r}_{det}(i)$ with $\mathbf{r}_{t-1}(i)$.
    Compute mean velocity $\boldsymbol{\nu}(i)$ within $\mathbf{r}_{t-1}(i)$ from the optical flow.
    if $\boldsymbol{\nu}(i) = 0$ or neither $\mathbf{r}_{bg}(i)$ or $\mathbf{r}_{det}(i)$ exists **then** Enter extrapolation mode.
    else
      $\mathbf{R}_{bg} = \mathbf{R}_{bg} \setminus \mathbf{r}_{bg}(i), \mathbf{R}_{det} = \mathbf{R}_{det} \setminus \mathbf{r}_{det}(i)$.
      Make measurement for tracking update $\boldsymbol{z}_t(i) = [\mathbf{r}_{bg}(i), \mathbf{r}_{det}(i), \boldsymbol{\nu}(i)]$.
      Set measurement covariance error R.
      Update object tracker with $\boldsymbol{z}_t(i)$ and R, get result $\mathbf{r}_t(i)$.
    CheckExitHeuristic(O_i)
  for each remaining box candidate $r \in \{\mathbf{R}_{bg} \bigcup \mathbf{R}_{det}\}$ **do**
    CheckEntryHeuristic($\mathbf{r}$).

Algorithm 2 CheckExitHeuristic(O)

if Object O is in extrapolation mode more than 50 frames **then**
  exit object O.

Algorithm 3 CheckEntryHeuristic($\mathbf{r}$)

if r is larger than 10×10 **then**
  initialize object.

used. BG uses background subtraction and optical flow, DET uses the object detector and optical flow, and BG+DET uses all three inputs. We also run several state-of-the-art trackers, including KCF (10), STRUCK (12), ASMS (11), DAT(13), staple (26), MEEM (27) and SRDCF (28) as baselines. Since all these trackers require manual initialization (namely human input), they are not able to be compared with our tracker directly. Instead, we can only partially evaluate them by providing manual initialization, see §2.5.4. By carefully selected manual initialization, the comparison here is in favor of the baselines.

2.5.2 Evaluation metrics

Given a set of generated and ground truth object trajectories, usually represented by a sequence of rectangular bounding boxes, we desire one or more performance metrics that capture the accuracy of the proposed system. Aspects that need to be captured include 1) tracking duration—if a ground truth trajectory of an object contains N frames, for how many of these frames does the system track the object, 2) recall—how many of the ground truth trajectories were represented in the tracking result, 3) precision—what proportion of tracking results had a corresponding trajectory, as well as 4) the overlap between the tracking result and the ground-truth.

Note that our problem does not fit into common multi-object tracking setting, since moving objects are tracked individually, instead of being modeled globally. Common metrics such as MOTA (29) would generate a meaningless number since we could have potentially more objects tracked than ground truth.

As the first step, we match each ground truth to a tracking result, by maximizing the accumulated overlap ratio r,

$$r = \frac{\sum_t (S_t^{gt} \cap S_t^{traj})}{\sum_t (S_t^{gt} \cup S_t^{traj})}, \tag{2.8}$$

where S_t^{gt} and S_t^{traj} are ground truth and trajectory box areas at frame t, respectively. Note that the sum is computed over the union of trajectory and ground truth lifetime. Equation 2.8 ensures the ground truth is matched to a longer trajectory with reasonable coverage. Additionally, to filter some spurious objects slightly touched the ground truth, we also require any match to have more than 30% overlap on at least one frame, where the value is set experimentally.

2.5.3 Object-level evaluation

Given the matched results, we can calculate the proportion of ground truth trajectories that were matched to the tracking result (recall), and the proportion of tracking results that had a matching trajectory (precision), for our three trackers and two types of videos. Figure 4 and Figure 5 show the results in absolute numbers, also to provide some perspectives on the scale of the evaluation. The true positives are those correctly tracked objects and false positives are noisy objects. Our best tracker configuration, BG+DET, achieves 81% recall and 87% precision on our low resolution, simple videos, and 65% recall, 57% precision on the high-resolution, complex scenes. Here, the majority of failures in the complex scenes were due to complicated interactions and heavy occlusion throughout the scene, where vehicles were only

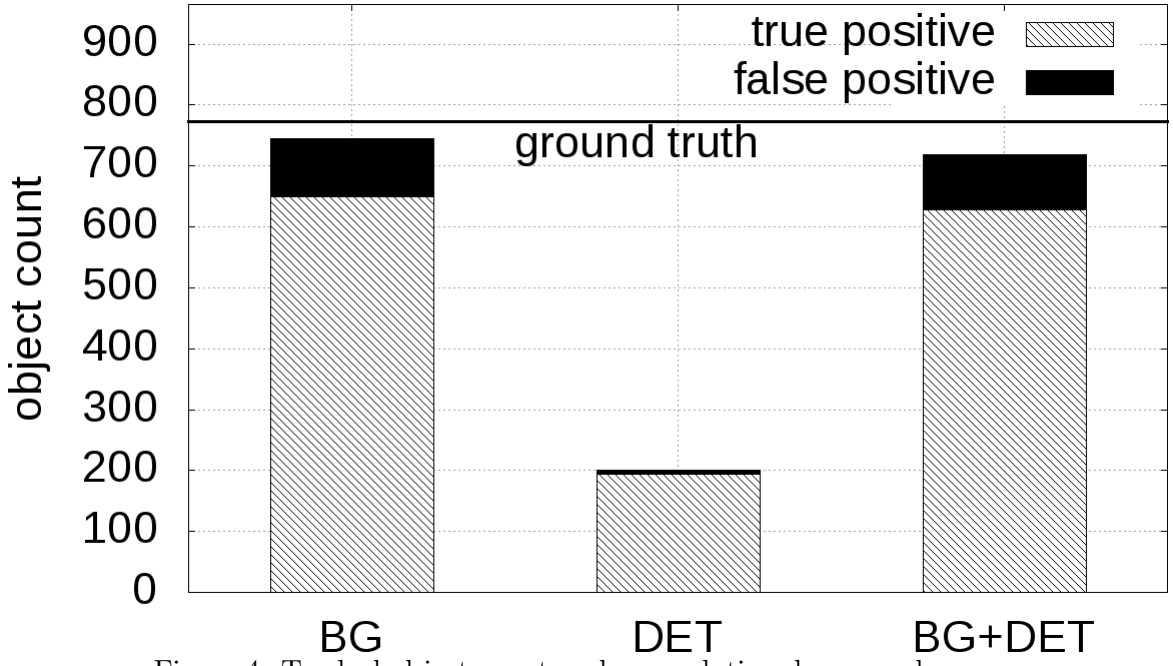

Figure 4: Tracked object count on low resolution, less complex scenes.

partially visible. Currently, we do not split such merged objects into their constituent parts; we leave this for future work.

Comparing the three configurations, we see that the detector performs quite poorly on the low-resolution scenes, due to small and poor quality imagery where it is sometimes difficult even for a person to correctly identify an object as a vehicle. By contrast, background subtraction does quite well on these uncomplicated scenes. For the more higher resolution complex scenes, the detector performs well, while the background subtraction model struggles and largely introduces noise.

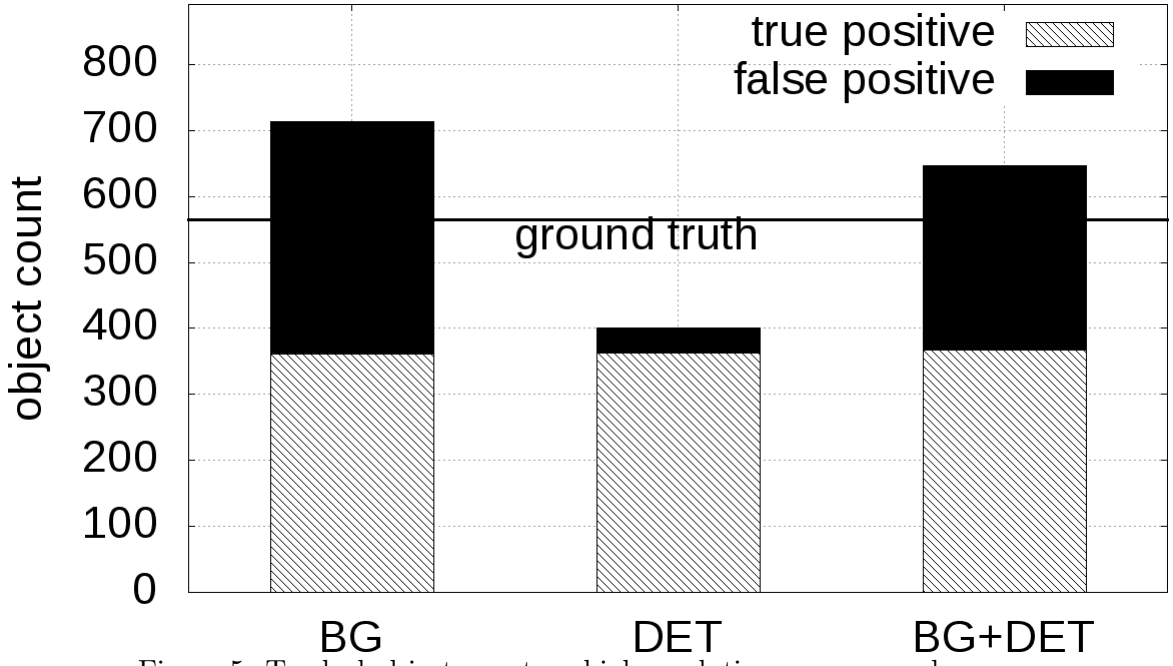

Figure 5: Tracked object count on high resolution, more complex scenes.

2.5.4 Pixel-level evaluation during entire lifetime

We are also interested in evaluating how well the tracker follows objects in the scene. For example, as one of our motivating application, accurate tracking is necessary for correct turning movement classification, as Figure 28a illustrates. While there exists no similar work or benchmark that incorporates automatic initialization, we can only partially compare our system to prior work. Here, we modify our tracker to accept manual initialization. Both our modified trackers and the baseline trackers are initialized with boxes extracted from ground truth. These "initialized" trackers are then evaluated along with our automatically initialized

trackers. Note that the experiment is designed in favor of those manually initialized trackers, since the initialization boxes are from ground truth and perfectly match the object in the scene.

To accept manual initialization in scenes with significant scale change, each tracker is initialized with the first box of ground truth larger than a threshold:

$$S_{thresh} = \left[\max(S^{gt}) - \min(S^{gt})\right] * s + \min(S^{gt}), \tag{2.9}$$

where $\max(S^{gt})$ and $\min(S^{gt})$ are the maximal and minimal ground truth areas along the sequence. $s \in \{0, 0.2, \ldots, 1.0\}$, corresponds to the minimum fraction of the maximum object size at which initialization may occur. Note s only affects objects that enter with an increasing size; while shrinking objects would be initialized upon appearance regardless of the threshold. Tracking is terminated at the last frame of ground truth. We arrived at this design as some trackers tend to perform poorly when initialized by small images, yet delaying initialization until the object grows large can result in arbitrarily shortened trajectory.

Figure 6 and Figure 7 compare the overlap ratio of our three tracker configurations both with manual and automatic initialization (horizontal lines), as well as the overlap ratio of several other trackers on our high- and low-resolution datasets. The x-axis is the initialization threshold s in Equation 2.9, and the y-axis is the overlap ratio r from Equation 2.8, averaged over all objects. This is computed from the first to the last frame of ground truth for the manually initialized and terminated trackers. While for our automatic trackers, it is computed over the

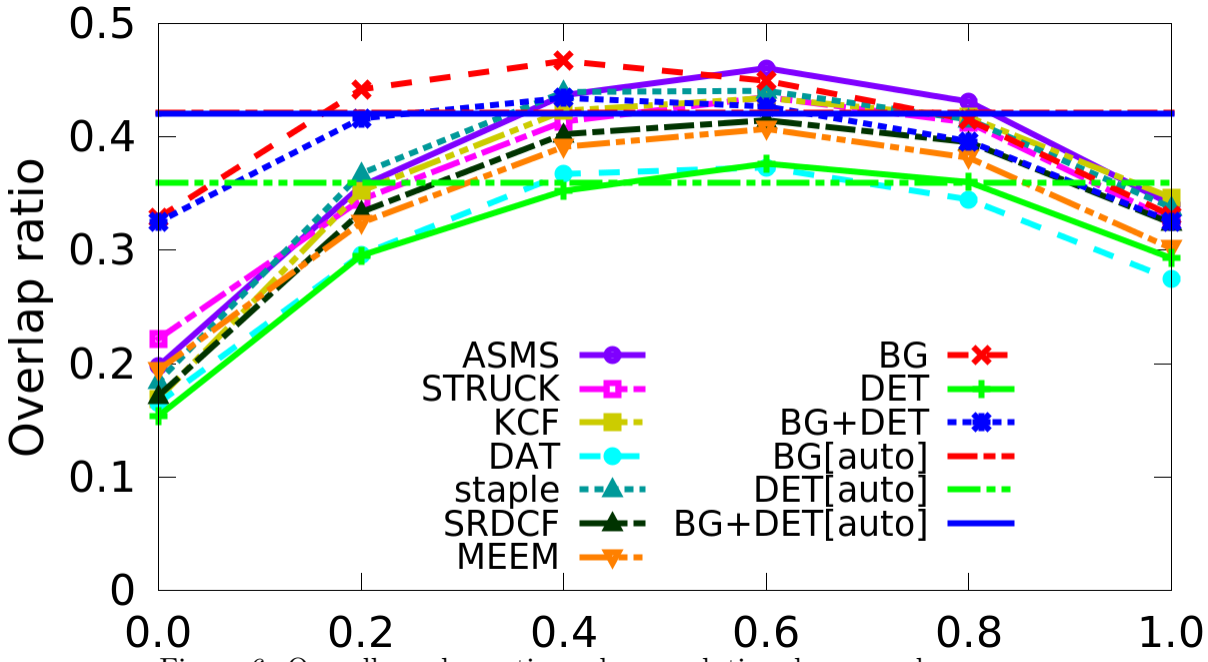

Figure 6: Overall overlap ratio on low resolution, less complex scenes.

union of tracking and ground truth lifetimes. This accounts for both tracking accuracy and lifetime, as we illustrated before.

The shape of the curves for the initialized trackers captures the trade-off between early-and-inaccurate, vs. late-but-accurate initialization. Overall, our BG-based trackers handily outperform other trackers when manual initialization and termination is provided. More importantly, the auto-initialized BG trackers essentially meet the performance of other trackers on the simple videos, and significantly outperform them on the complex videos. We hypothesize that the automatic initialization allows the tracker to better adapt to individual vehicles vs. the constant threshold set for manual initialization. Additionally, consistent with our conclusion

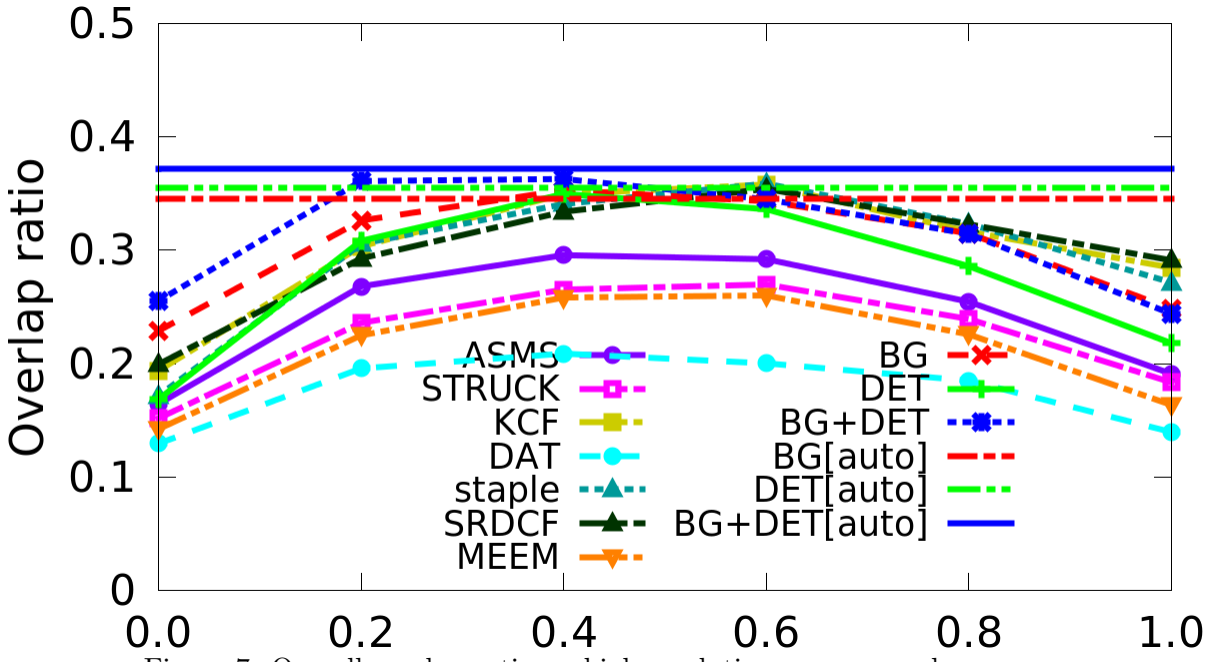

Figure 7: Overall overlap ratio on high resolution, more complex scenes.

in §2.5.3, detector dominates the tracking update on high resolution videos, while background subtraction plays its role on low resolution videos.

2.5.5 Pixel-level evaluation during tracked period

Then we focus on the performance during only the tracked period. Borrowed from standard single object tracking measurement, we show the success plot for trackers for two video groups, in Figure 8 and Figure 9. Different from above, we compute the success frame rate from the initialization frame, instead of entire ground truth sequence. The performance is measured by the area under the curve. By Figure 6 and Figure 7 we see overlap ratio between 0.2 and 0.6 is a good balance of tracking accuracy and trajectory completeness, we hereby show results

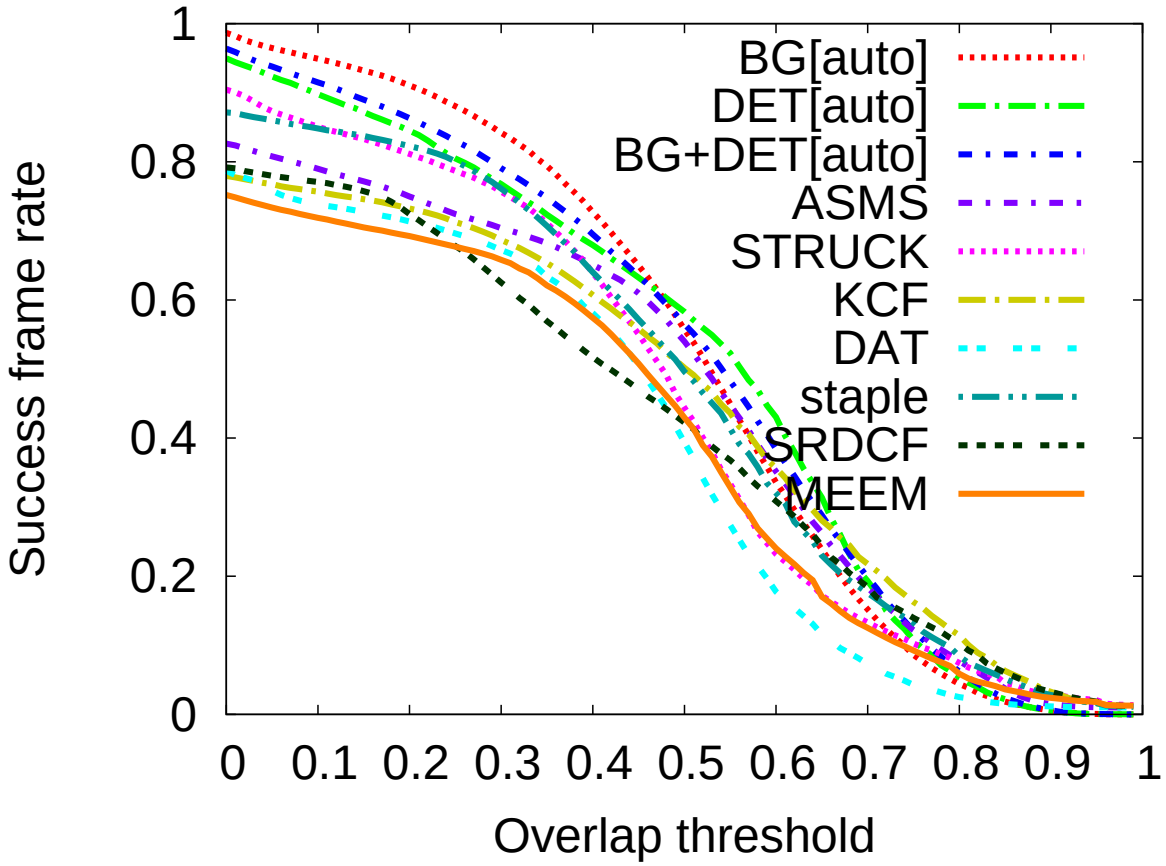

Figure 8: Success plot of low resolution, less complex scenes.

of initialization threshold of 0.4 here. Our automatic trackers significantly outperform other trackers with manual initialization. This demonstrates that proper initialization is critical to the tracking performance and similar conclusion about the contribution of each tracking component can be drawn.

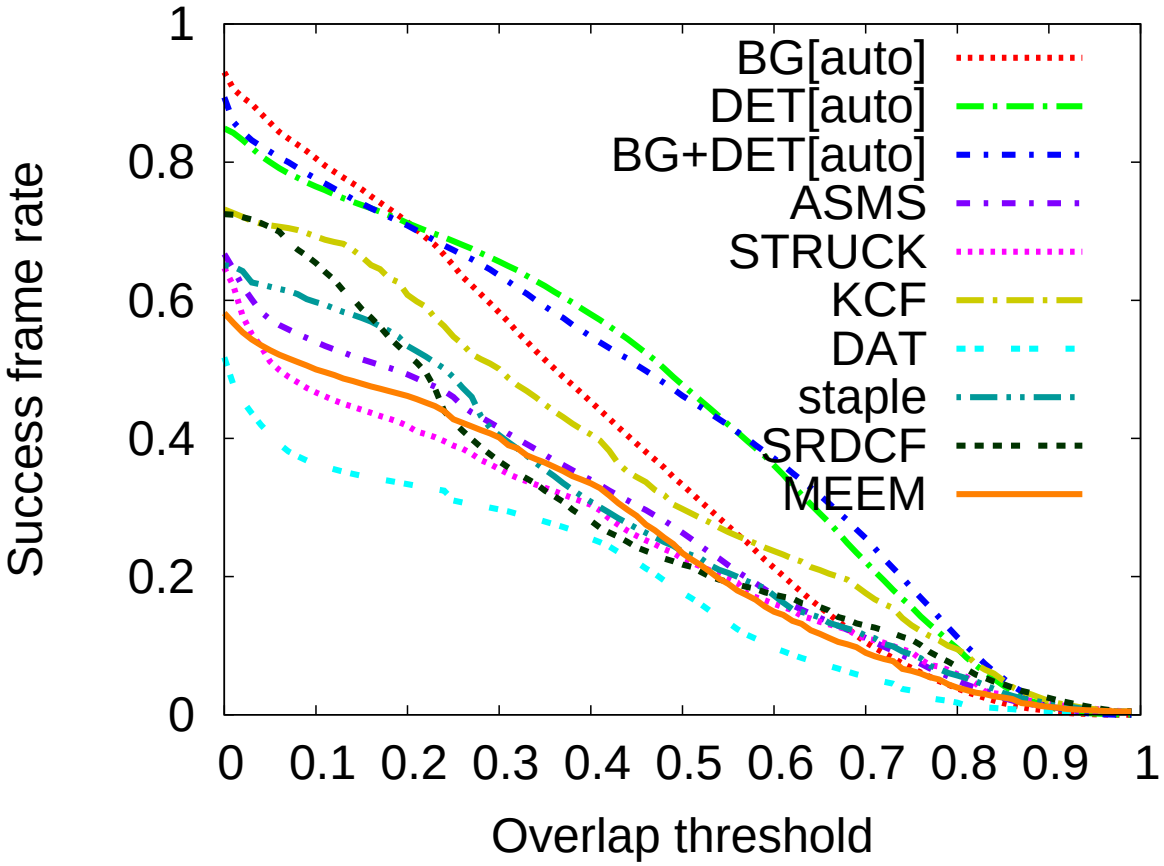

Figure 9: Success plots of high resolution, more complex scenes.

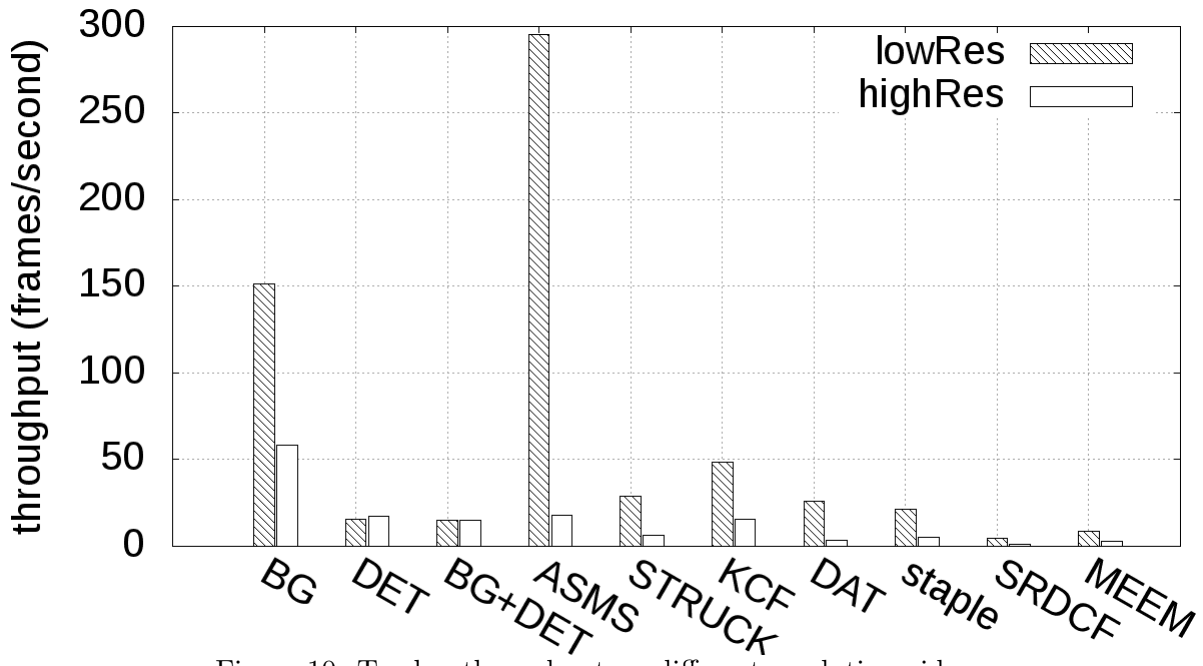

Figure 10: Tracker throughput on different resolution videos.

2.5.6 Throughput

Finally, we explore the throughput of trackers on different resolution videos, as shown in Figure 10. The evaluation was done on a Linux desktop with an Intel Core i7-3770 3.40GHz processor and a GeForce GTX TITAN X GPU. According to these results, BG significantly outperforms 6 out of 7 baseline trackers, with around 5× throughput improvement compared with real time (about 30 fps). Interestingly, ASMS outperforms our BG tracker on low resolution videos, however, it becomes 17× slower once it is applied on high resolution videos. Although the use of the object detector (DET, BG+DET) makes the tracker slower, they are the only

ones that maintain a similar frame rate on both low- and high resolution videos near real time, showing good scalability of resolution.

2.6 Related work

Object tracking: Object tracking algorithms fall into either multi-object or single object tracking category. Multi-object trackers deal primarily with the combinatorial task of associating sets of detections across frames, often modeled as a graph-based global optimization problem (30; 31). Such methods are computationally expensive, and typically impractical in time-critical applications. Meanwhile, single object tracking has experienced a rapid progress with the help of robust feature representation (32) and better learning scheme such as SVM (12) and boosting (33). However, object tracking still remains a challenging problem due to the difficulty caused by changing appearance and occlusions. To cope with appearance change, better affinity measurement (34) and adaptive learning schemes (35) may help. For occluded objects, multi-object trackers tend to inherently model occlusion, for example, using augmented graph representation (30) while single object trackers maintain the memory of the object appearance (35).

Tracker initialization and termination: Trackers today are evaluated in an idealized setting, where manual initialization and termination is provided. Most multi-object trackers assume excellent detector performance, but do handle object entry/exit. They either model it intrinsically by adding entry/exit nodes to the optimization graph (36), or manually by defining an entry and exit area (37). In (25), the only available literature we found related to tracker initialization, the authors evaluate single-object tracker initialization spatially and temporally,

and conclude that spatial and temporal variation of initialization would affect the tracking performance. However, no conclusion on how to make proper initialization is made.

Vision in traffic surveillance: Recently computer vision techniques are extensively applied in traffic analysis with the wide deployment of surveillance camera, such as real-time vehicle tracking (38), vehicle counting (39), parking occupancy detection (40), anomalous event detection (41). Compared with core computer vision algorithms, such systems face more real-world challenges and restrictions. Therefore manual input is often added to achieve reasonable performance. For instance, image–real world coordinates mapping beforehand (38), lane width on image (42), and entry region for vehicle detection (42). Another observation is that those systems are only applicable to videos of a certain view. For example, (38) uses top-front view of high way videos, making vehicles roughly the same size. Therefore, the portability is significantly limited by manual input and task-specific applications.

CHAPTER 3

SCENE LEARNING

3.1 Introduction

For a traffic camera mounted at a static location, objects in the recorded videos move along the road geometry with a regular pattern. Those movement patterns could be useful for video analysis. For example, objects that do not follow the usual movement pattern are likely to be anomalous; therefore, they are worth special attention. Besides, statistics on different movements provide analysis on a finer granularity. For example, Illinois Department of Transportation (IDOT) keeps track of the vehicle counts in different moving directions, for traffic cameras all across Illinois.

It is usually intuitive for a human to identify the movement patterns after watching such a video for a while. However, human's interpretation lacks a mathematical representation and may vary among different people. Also, people are prone to making mistakes when dealing with complex videos; their performance may tend to decrease with longer working hours.

As a result, it is essential to automate this process for fast and large scale processing. Some researchers are working on clustering existing trajectories and obtain a semantic representation of the scene (43; 44). However, such a method is usually sensitive to noises. More importantly, it is often hard to get clean trajectories via object tracking algorithms. An additional step of data cleaning is necessary to make the clustering method work. On the other hand, compared

with object-level trajectories across multiple frames, pixel movement on individual frames is a more robust input for the scene understanding problem. It excludes the interference of object interaction and forms a lower-level summary of the scene. In this chapter, we apply a non-parametric clustering method (45) to learn the vehicles' movement pattern in an unsupervised manner. The resulting clusters have a mathematical representation in the form of a set of distributions; therefore, they are easier to interpret in the subsequent processing.

3.2 Atomic motion extraction

Tracking performance can be improved with the help of scene semantics. For example, objects may have nonlinear changes in their sizes and speeds as they move due to camera perspectives, and characterization of such non-linearity can regulate and benefit the tracking of the objects. We propose an unsupervised framework, as shown in Figure 11, to capture and exploit these constraints. First, to capture global and long-range trajectories with rich semantics, local motion patterns of smaller units, such as fine-grained grids, are extracted (step 1). We capture the local motion directions, which can be different but spatially interdependent across the grids, via a non-parametric topic model called HDP (46; 45). For any scene, the model flexibly captures any local motion directions, which are mixtures of base directions, without human presuming a universe of patterns. Then, we synthesize global trajectories from the local patterns (step 2). Specifically, we adopt the trajectory finding algorithm from (45) but improve it by: (i) identifying multiple significant trajectories rather than a single one, and (ii) sampling multiple possible instances from the same underlying trajectory to capture richer geometric information rather than a single line. The sampled instances reveal key information

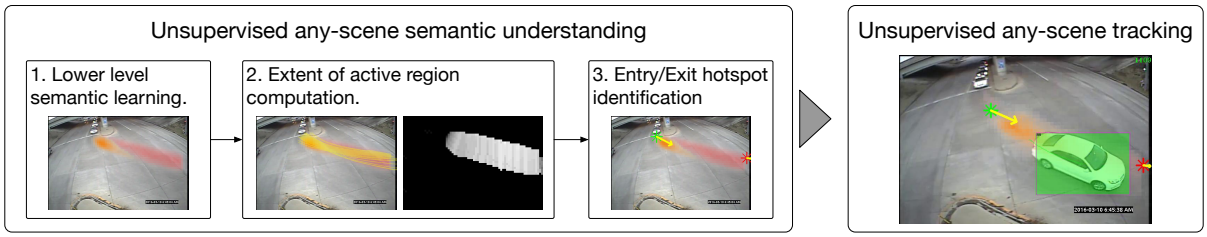

Figure 11: System overview. The left corresponds to scene learning module: frequent motions are extracted in an unsupervised fashion, then the active regions where most objects move are learned on top of the motion result. Next, the entry/exit hotspot and their direction are extracted, describing how most objects enter and exit the scene. On the right, the semantic knowledge is applied to a tracker.

for tracking: (i) hotspots where vehicles enter and exit the scene; and (ii) the extent in the direction perpendicular to the principal direction (namely the direction from the starting to the ending point) that changes nonlinearly but smoothly along that trajectory. Lastly, we integrate the discovered hotspots and trajectories in a tracking model as constraints to significantly reduce the false positives with improved or comparable false negatives.

3.2.1 Non-parametric clustering via HDP

For the general purpose of scene learning, lower-level representation could be a much more robust feature due to the difficulty of obtaining an accurate higher-level result, such as consistent object trajectories. A cluster of such low-level data as pixel movement could be an informative summary. Inspired by the previous work (45; 47), motion patterns can be learned by topic model, with an analogous bag-of-words representation to document classification.

Videos are processed as described in Figure 12: first every frame is divided into small grids — small enough to have consistent optical flow results. To distinguish different motions,

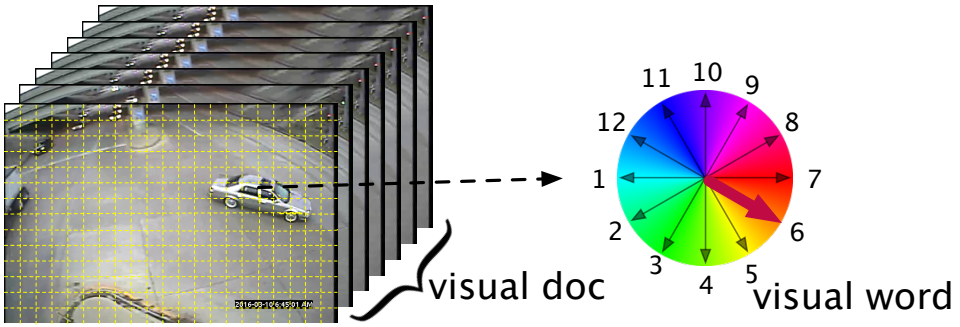

Figure 12: Left column illustrates the spatial and temporary quantization of video frames. The right shows a visual word obtained by discretizing the optical flow direction.

optical flows of consecutive frames are quantized on D directions after some simple filtering (24). Making an analogy with to document clustering, on a certain frame, each optical flow at a grid coordinate (x, y) on a quantized direction is a *visual word*. If the frame is divided into $w \times h$ grids, the vocabulary is $V = w \times h \times D$. As shown in the middle column of Figure 12, the videos are then split temporarily into short video clips. Each video clip has enough frames to contain a complete motion, at the same time, is not too long to have mixed motions. By counting the number of visual words on each grid and each quantized direction in every video clip, we have a bag-of-words representation of *visual documents*. Similarly, a cluster trained from the video could be called *visual topic*.

Using the bag-of-words representation, motions could be learned by any existing topic model method. In most clustering methods, the number of clusters is required as an input, and the results usually vary accordingly. For complex videos, it is presumably hard for people to identify the number of major motions. Therefore the non-parametric clustering method —HDP is used.

It is a generalization of Dirichlet Process (DP), requiring no specification of the cluster number. In this model, visual words contain groups of observations, each exhibiting a mixed proportion of shared mixture components. The mixture components are learned in this model, also called "topics". More specifically, an HDP is a two-level DP with shared parameters. Each group j is associated with a draw from a shared DP whose base distribution is also a draw from the top-level DP.

$$\begin{aligned} G_0 &\sim \mathrm{DP}(\gamma, H) \\ G_j | G_0 &\sim \mathrm{DP}(\alpha_0, G_0), \text{for each } j, \end{aligned} \tag{3.1}$$

Here j is the group index. At the top-level, the distribution G_0 is drawn from a DP with concentration parameter γ and base distribution H. The base distribution H is a symmetric Dirichlet over the vocabulary simplex. Each atom is a distribution over the vocabulary, the atoms $\boldsymbol{\phi} = (\phi_k)_{k=1}^{\infty}$ are drawn independently $\phi_k \sim \mathrm{Dirichlet}(\eta)$. Since the numbers drawn from a Dirichlet distribution sum up to 1, they are usually used as the parameters of a multinomial distribution. Simply speaking, G_0 is a discrete distribution over the atoms $\boldsymbol{\phi}$. At the bottom level, G_0 is used as the base distribution to draw each group distribution G_j, each is another multinomial distribution over the atoms $\boldsymbol{\phi}$. By such hierarchical definition, the atoms are shared among G_j, which makes sense that different documents may belong to the same topic.

In our setting, a group is a visual document and the ith word of the jth document x_{ji} is drawn as follows:

$$\theta_{ji} = \phi_{z_{ji}}, \quad \theta_{ji} | G_j \sim G_j, \quad x_{ji} | \theta_{ji} \sim \mathrm{Multi}(\theta_{ji}) \tag{3.2}$$

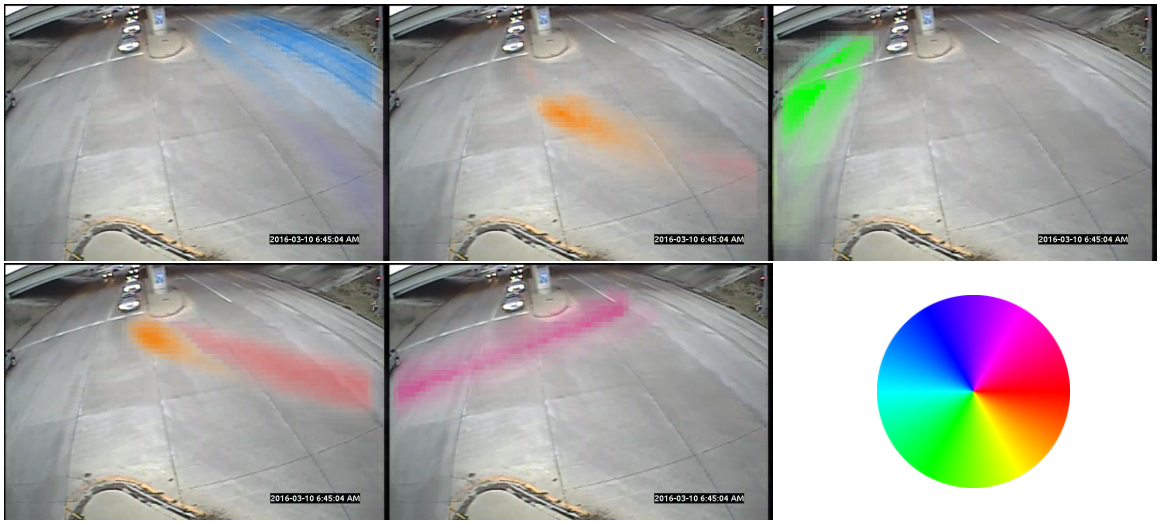

Figure 13: Motions learned by HDP, colors indicate directions as the color wheel shows, the lightness indicate the magnitudes of the maximal probability values..

Here z_{ji} is the topic assignment of x_{ji}, each word is associated with a multinomial distribution θ_{ji} according to its topic z_{ji}. We could potentially have an infinite number of atoms. However, only a finite number of atoms/topics are learned. After Gibbs sampling, there is a multinomial distribution for each topic over the vocabulary where each word in a document has a topic assignment. In other word, words in the same document may belong to *different* topics. Figure 13 visualizes those topics learned by HDP. The color indicates the direction shown in the color wheel on the right and the lightness indicates the value of the multinomial at the corresponding grid. The Figures show that HDP does an excellent job of summarizing the motions in the video, even without knowing any moving objects in the scene. For more details on the model and Gibbs sampling, please see (46).

3.3 Semantic knowledge learning

The results generated by HDP are several clusters of visual words, however, without any semantic meaning. This section describes some post-processing steps for extracting higher-level semantic knowledge of the camera scene.

3.3.1 Robust ridge climbing

Just by looking at the topics in Figure 13, we could roughly infer how the vehicles move in the video. More importantly, the extent of the high-density grids gives useful insights into the size and moving region of the tracked objects. Let ϕ be a multinomial distribution of a topic learned by HDP. For any grid i, it has D values, corresponding to D evenly quantized directions, written as $\boldsymbol{\phi}_i = [\phi_i^1, \phi_i^2, \ldots, \phi_i^D]$. We define two terms: $d_i^* = \arg\max_d(\phi_i^d)$ is the *dominate direction* of grid i, which has the maximal value of distribution among all directions. We also define a terms summing over all the directions of each grid $\varphi_i = \sum_{d=1}^{D} \phi_i^d$. Figure 15a shows an example of the distribution of a particular topic on a grid, where the radius of each sector indicates the value of ϕ_i^d. In this topic, the grid has the highest ϕ_i^d with $d = 1$, indicating that it will be most likely to move along this direction. Figure 14 gives a 3D visualization of the first topic in Figure 13, where the height at each grid is φ_i. Overall they form a mountain-like surface. We aim to learn the shape and extent by extending the ridge climbing method in (48). The idea of this method is to start from a high-density grid, make one step iteratively until reaching the image boundary or the low-density area. The steps move along the desired direction and follow the shape of the topic distribution. For consistency, all the following examples are on the first topic in Figure 13.

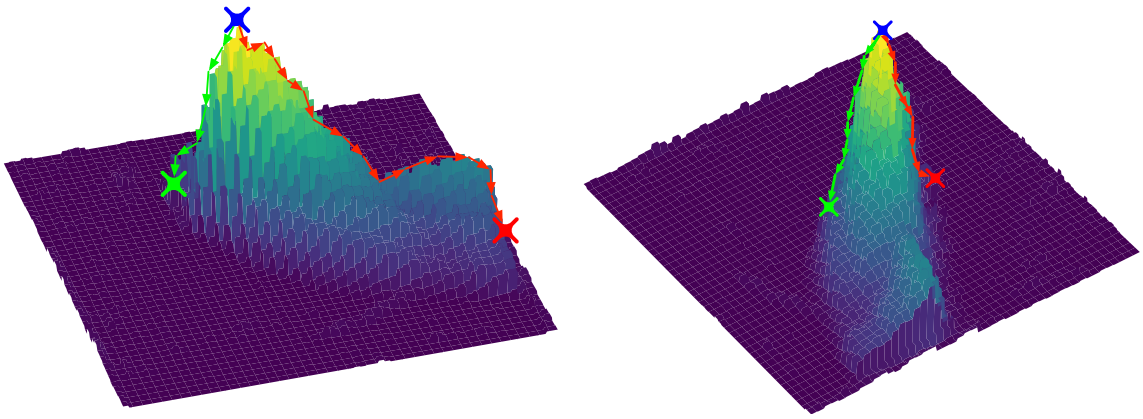

(a) (b)

Figure 14: Ridge climbing methods on a topic distribution: along the most likely topic direction (a) and its perpendicular direction (b). Blue cross indicates the starting point, red and green point indicates the end point.

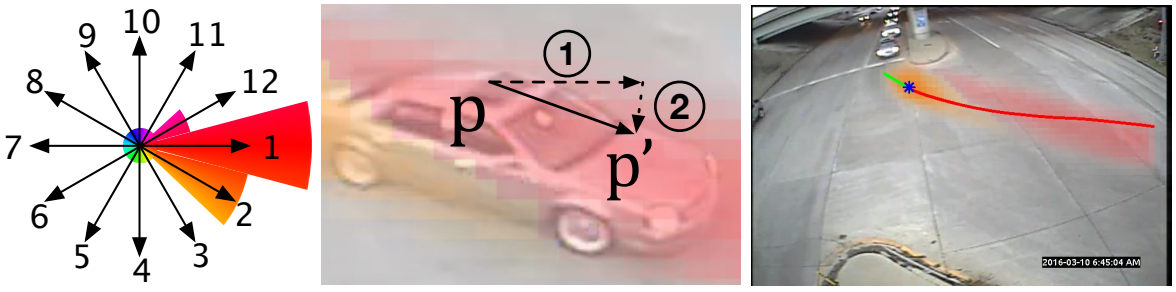

(a) (b) (c)

Figure 15: a is an example of the topic distribution on one grid, where the radius of each circle sector indicates φ_t^1. b shows the move-adjust step of each iteration. c is an extracted ridge starting from the highest density grid, where the blue star indicates the highest density grid, green and red line indicates ridges to the start/end point separately.

We propose a two-step movement in each iteration: first, we take a step, the step size is the normalized mean density on all the direction in its neighborhood; second, we adjust the step by moving toward higher density area. The above steps are illustrated in Figure 15b, represented in dash lines, the final step is in solid line. Mathematically, the two-step movement from $\mathbf{p}$ to $\mathbf{p^*}$ is represented as:

$$\mathbf{p}' = \mathbf{p} + \frac{\boldsymbol{\nu}}{||\boldsymbol{\nu}||_2}, \qquad \boldsymbol{\nu} = \frac{\sum_{i=1}^{n} f(\boldsymbol{\omega}) \cdot \boldsymbol{\phi}_i}{\sum_{i=1}^{n} \varphi_i}, \tag{3.3}$$

$$\mathbf{p}^* = \mathbf{p}' + \alpha \cdot \mathfrak{m}, \qquad \mathfrak{m} = \frac{\sum_{j=1}^{n} \varphi_j \times (\mathbf{p}_i - \mathbf{p}')}{\sum_{j=1}^{n} \varphi_j}. \tag{3.4}$$

We define a $2 \times D$ matrix $\boldsymbol{\omega} = [\boldsymbol{\omega}_1, \boldsymbol{\omega}_2, \ldots, \boldsymbol{\omega}_D]$, each column $\boldsymbol{\omega}_d$ is the unit vector along the quantized direction d. $\boldsymbol{\nu}$ and $\mathfrak{m}$ correspond to the move and adjust step, separately. For the move step Equation 3.3, $f(\boldsymbol{\omega})$ defines movement of each $\boldsymbol{\omega}_d$ wrt. a desired moving direction, which is the same size with $\boldsymbol{\omega}$. Here we choose a neighborhood with n grids around $\mathbf{p}$, and $\mathbf{p}_i$ is the coordinate of the ith grid in the neighborhood. Therefore, $f(\boldsymbol{\omega}) \cdot \boldsymbol{\phi}_i$ is the mean direction weighted by densities on each direction. However, the moving step may not follow the elongated shape of the topic due to the uncertainty introduced by the quantized direction, where an example is given in Figure 15b. To deal with it, we make an adjustment on the result of the move step Equation 3.4, once reaching a lower density area, $\mathfrak{m}$ pulls the point back to the higher-density area and make the final step (solid arrow in Figure 15b) better follow the shape of the topic, as illustrated in step 2 in Figure 15b. Note that in the adjust step, we compute a new neighborhood around the result of the move step. Intuitively, if we reach a grid

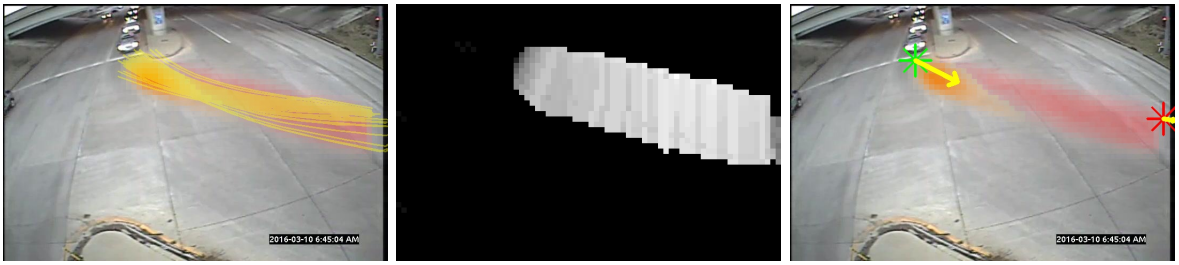

(a) (b) (c)

Figure 16: a: multiple ridges learned from local maximal grid. b: perpendicular width, where lighter intensity indicates a larger width. c: extracted entry/exit hotspots indicates by the green and red star. And the yellow arrow shows their direction.

that has significantly different densities, we tend to take a smaller step in case the step size is too large to follow the density surface. On the contrary, if the first step reaches a grid with a roughly uniform distribution around, $\mathfrak{m}$ tends to be a zero vector and does not affect the final step. Due to the normalization term, $\boldsymbol{\nu}$ and $\mathfrak{m}$ has magnitude at most 1 in (Equation 3.3) and (Equation 3.4). To make sure the adjust step does not cancel out the movement of step one, we normalize $\boldsymbol{\nu}$ into a unit vector. By setting $\alpha \in (0, 1)$, it has a fixed impact on the final step. We observe that $\alpha \in [0.1, 0.2]$ gives a reasonable result.

Figure 14a gives an visual illustration of the ridge climbing process along the dominant direction, and Figure 15c shows the resulting ridge. The process starts from the grid with the highest φ, indicated by the blue cross, along the dominant direction, in this case, direction 1. The red line is the path to the end point of the ridge, with $f(\boldsymbol{\omega}) = \boldsymbol{\omega}$; while the green line reaches the start point, obtained by setting $f(\boldsymbol{\omega}) = -\boldsymbol{\omega}$. So far the results are similar with those in (48).

3.3.2 Topic extent learning

Intuitively, the high-density grids indicate an active region when objects are more likely to move. A single ridge is not descriptive enough, especially for wide motion regions. We propose two variations of the above procedure. First, instead of starting from the grid with global maximal φ, we start with multiple grids with local maximal φ in its neighborhood. The yellow lines in Figure 16a show the ridges extracted by the above procedure, where they roughly cover the high-density area. Second, we define a *perpendicular width* as the extent of the high density grids that perpendicular to the dominate direction. To obtain it, we climb the density surface along the direction perpendicular to the dominate direction d_i^* of the current grid i, demonstrated in Figure 14b. $f(\boldsymbol{\omega})$ is obtained by rotating each unit vector $\boldsymbol{\omega}_d$ by 90 degrees clockwise ($f_1(\boldsymbol{\omega})$) and counterclockwise ($f_2(\boldsymbol{\omega})$). In other words,

$$f_1(\boldsymbol{\omega}) = \begin{bmatrix} 0 & -1 \\ 1 & 0 \end{bmatrix} \cdot \boldsymbol{\omega}, \quad f_2(\boldsymbol{\omega}) = \begin{bmatrix} 0 & 1 \\ -1 & 0 \end{bmatrix} \cdot \boldsymbol{\omega}.$$

Figure 16b shows the learned perpendicular width of the same topic, where the lighter color indicates a larger width. The ridges and the perpendicular width together define the active region of a topic, giving size, location and direction of the belonging objects.

3.3.3 Entry/exit hotspots extraction

Compared with a single ridge, ridges start from multiple locations and better indicate the start and end of motions due to their larger coverage. The density of extracted ridges gives a nice interpretation of the area and it is unlikely for vehicles to go beyond the topic area. For

a set of ridges $\{\mathbf{l}_1, \mathbf{l}_2, \ldots, \mathbf{l}_m\}$, each of $\mathbf{l}_i$ is a sequence of grid coordinates $\mathbf{l}_i = \{\mathbf{p}_i^1, \mathbf{p}_i^2, \ldots, \mathbf{p}_i^{s_i}\}$, where s_i is the length of ridge $\mathbf{l}_i$. We take the first and last point of each ridge, call them *candidates* of the entry/exit hotspot. Formally defined as

$$\mathbf{Z}_{\text{entry}} = \{\mathbf{p}_1^1, \mathbf{p}_2^1, \ldots, \mathbf{p}_m^1\}, \quad \mathbf{Z}_{\text{exit}} = \{\mathbf{p}_1^{s_1}, \mathbf{p}_1^{s_2}, \ldots, \mathbf{p}_1^{s_m}\}.$$

Similarly, each has its own direction:

$$\begin{aligned}\mathbf{V}_{\text{entry}} =& \{\mathbf{p}_1^2 - \mathbf{p}_1^1, \ldots, \mathbf{p}_m^2 - \mathbf{p}_m^1\},\\ \mathbf{V}_{\text{exit}} =& \{\mathbf{p}_1^{s_1} - \mathbf{p}_1^{s_1-1}, \ldots, \mathbf{p}_m^{s_m} - \mathbf{p}_m^{s_m-1}\}.\end{aligned}$$

Averaging over the coordinations and directions of candidates, we have a mean location and direction for each entry and exit hotspot:

$$\mathbf{p}_{\text{entry}} = \frac{\sum_{i=1}^m \mathbf{p}_i^1}{m}, \quad \boldsymbol{\nu}_{\text{entry}} = \frac{\sum_{i=1}^m \mathbf{p}_i^2 - \mathbf{p}_i^1}{m}, \tag{3.5}$$

$$\mathbf{p}_{\text{exit}} = \frac{\sum_{i=1}^m \mathbf{p}_i^{s_m}}{m}, \quad \boldsymbol{\nu}_{\text{exit}} = \frac{\sum_{i=1}^m \mathbf{p}_i^{s_m} - \mathbf{p}_i^{s_m-1}}{m}. \tag{3.6}$$

16c gives an visual result of the above process, where the green and red star corresponds to $\mathbf{p}_{\text{entry}}$ and $\mathbf{p}_{\text{exit}}$, the yellow arrow shoes their directions $\boldsymbol{\nu}_{\text{entry}}$ and $\boldsymbol{\nu}_{\text{exit}}$. Although entry/exit hotspots are also able to be obtained by fitting the start/end points of trajectories, they are less reliable than statistics learned from lower-level representation, since we are working on a tracking framework.

3.4 Semantic knowledge visualization

For topic model training, we make each video clip 90 frames (~ 3 sec); each frame is divided into 10×10 pixel grids. Different from $D = 4$ in (45; 47), we make $D = 12$. This number considers motions more than horizontal and vertical, making subsequent post-processing more accurate. We extend a C++ implementation of HDP [1] and train the models on IDOT dataset (9), each video is around 5 minutes. In the following, we first give some examples of the scene learning results, then see how the semantic knowledge helps improve object tracking.

Complementing the partial results in previous sections, Figure 17, Figure 18 and Figure 19 provide complete results on several scenes, with the same representation as previous sections. Figure 17 summarizes a low-resolution video, where the four main motions are captured, however, some turning motions may be missed. This is likely because optical flow with small magnitude is filtered as error before it is fed to the topic model, or because such motions are rare or do not appear in the training video. For higher resolution videos, such as Figure 18 and Figure 19, optical flow results are more accurate and movement magnitudes are greater, when measured in pixels. Consequently, HDP can catch most visible motions, and even distinguish individual lanes. By visual inspection, the obtained movements, as well as the locations and directions of entry/exit points, are consistent with the subject scenes.

3.5 Future work

[1] Chong Wang, David Blei: https://github.com/blei-lab/hdp.

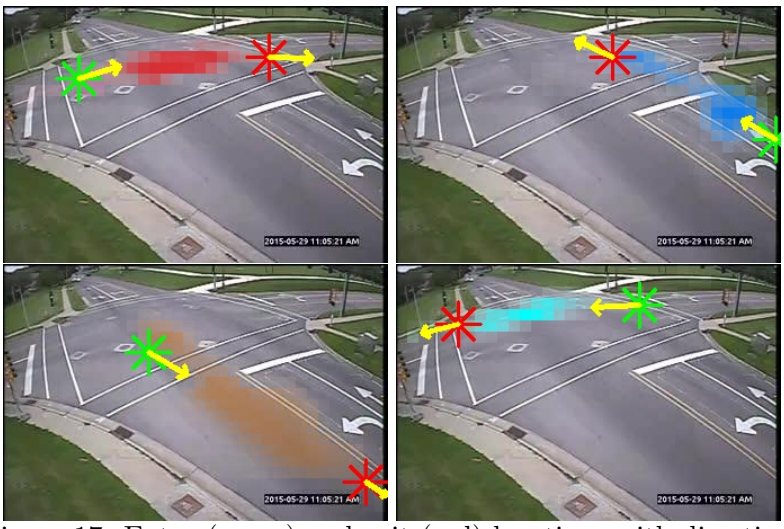

Figure 17: Entry (green) and exit (red) locations with direction.

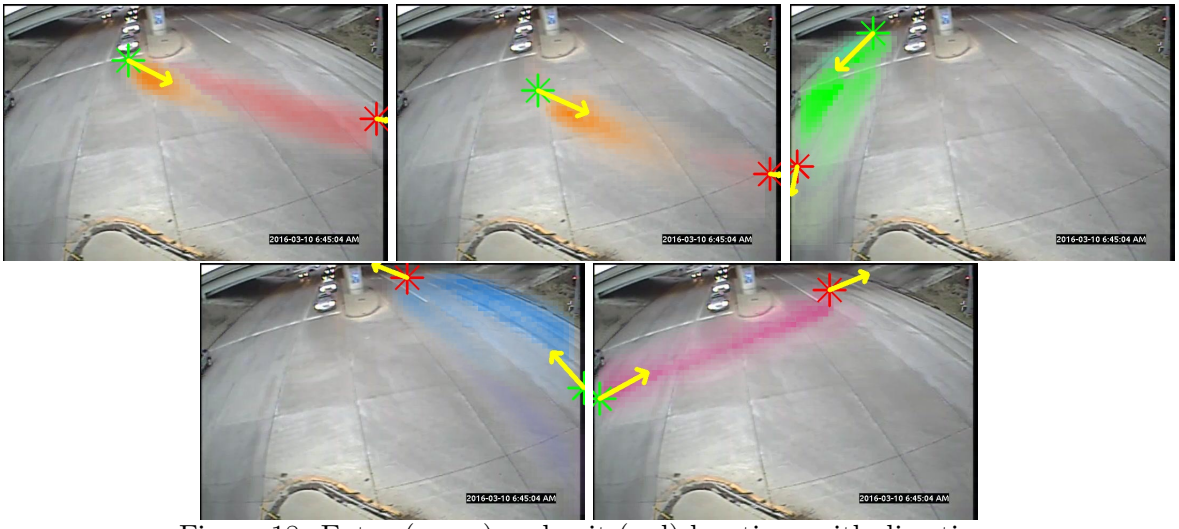

Figure 18: Entry (green) and exit (red) locations with direction.

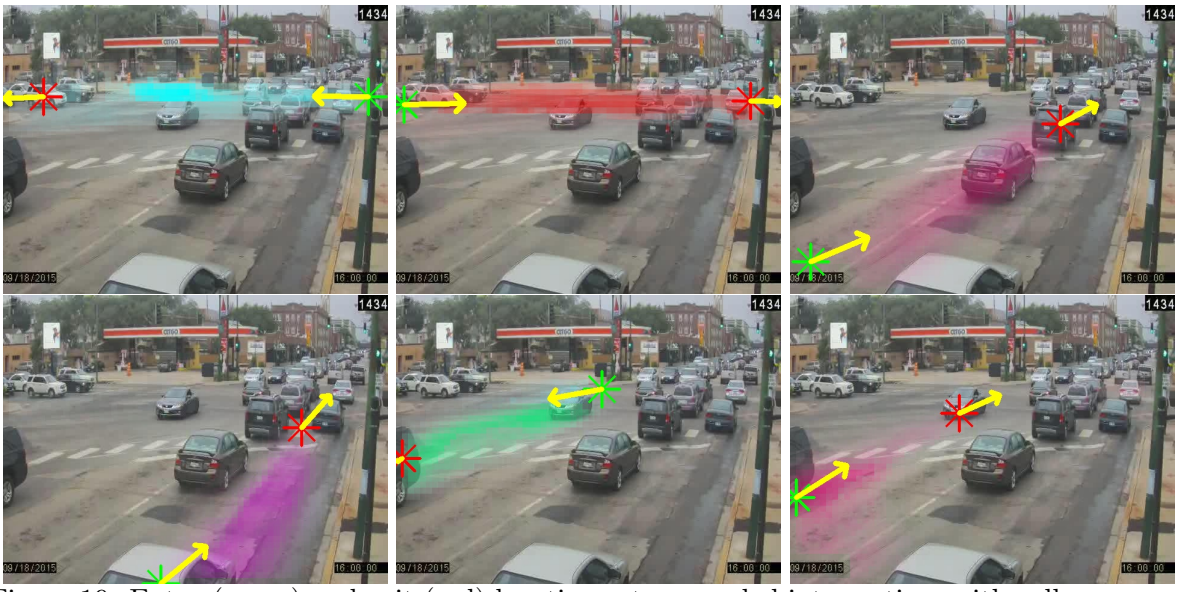

Figure 19: Entry (green) and exit (red) locations at a crowded intersection, with yellow arrows indicating their direction.

CHAPTER 4

SEMANTIC TRACKER

4.1 Introduction

Transportation videos are nowadays captured by millions of cameras installed at local and national highways and streets[1]. The analysis of such videos is critical for traffic volume monitoring, peak hour and congestion patterns discovery, tracing cars of criminals and stolen cars, highway toll management, among many others. For decades people have been trying to extract information from transportation surveillance videos. For example, one can hire a large number of human workers to watch and mark up any subregions, frames, or clips, that contain information of interest. This practice is labor-intensive and not scalable, as the workers need to pause from time to time and carefully analyze each object frame-wise. Even with high detection precision, recall can be low due to the bottleneck cheap human labor and processing bandwidth.

Recently, advanced solutions based on computer vision are proposed to mitigate the bottleneck but are still limited by human processing bandwidth and far away from fully automatic traffic surveillance. First, while precise specifications of capturing camera or the starting and ending points play a large role in tracking accuracy (9; 49; 50; 51; 52; 53), the videos are time-consuming to hand-labeled accurately with this level of details, while given a large number

[1]The Illinois Department of Transportation has a huge database of 24-hour traffic videos all across Illinois.

of cameras deployed nationwide, it is unwise to provide specifications for every camera. Second, any models trained for one scene cannot be deployed in other scenes, as the semantics of surveillance scenes, such as entry/exit area (49; 50) or road surface (54), can differ from scene to scene. Also, the same camera can undergo slight adjustments in their focus and angle, and a model trained for that camera can become inaccurate and incur further costly re-calibrations.

In this paper, we aim at fully automatic semantic knowledge extraction from transportation videos and significantly reduce human efforts in the vehicle tracking pipeline. A vehicle tracker can benefit from the more restricted motion patterns in traffic videos and we propose a video scene semantic learning method to discover atomic motions, the extent of active regions, entry/exit hotspots, etc.. We integrate the learned semantic knowledge into a tracker based on Kalman Filter, which can flexibly accommodate state-of-the-art object detectors like faster-RCNN (20). Experiments on 13 long surveillance videos with diverse tracking scenes demonstrate the significantly improved tracking accuracy attained the proposed method, compared with other fully automatic approaches.

Our preliminary contributions are as follows:

- Explicitly addressed those critical yet ignored issues for practical surveillance applications, such as automatic initialization and termination.
- Proposed a self-adaptive framework to where trackers are guided by the learned semantic scene knowledge, while in return the semantic knowledge is updated with tracking statistics.

- Provided a comprehensive evaluation of the proposed framework and demonstrate a significant improvement on object tracking.

4.2 Object motion assignment by online inference

After learning the semantic knowledge for visual topics, we have to identify the topic assignment of a tracked object before any topic-specific constraints could be applied. We used the off-line trained topic model to do inference on newly come videos for the same camera. For inference on a certain frame, first a small window of consecutive frames close to the current one is chosen and processed into bag-of-words representation, same with training videos in Section 3.2.1. After inference, each word has a multinomial distribution over topics, and it is assigned to the one with maximal probability. Assume that those frames contain consistent motions, we pick the most likely topic for each location. For a tracked object covering multiple grids, we simply use majority voting for each object within its extent to get its topic assignment. We omit the inference detail here, for details we refer the reader to (46).

4.3 Tracking score

Based on the life span of a tracked object, there are three stages: initialization, tracking, and termination. Most literature focuses on tracking, assuming initialization and termination are properly handled. However, for practical use, each stage should be carefully dealt with to ensure performance. For the first time, we introduce applying the scene-specific semantic knowledge to object tracking throughout the objects' lifetime.

(a) (b)

Figure 20: Two scenarios of object enters and exits: a: objects enter with a tiny size and move out of image boundary; b: objects enter from the image boundary and exit with a tiny size in within the frame. Green and red star are the obtained entry/exit hotspots; yellow arrows shows their direction.

4.3.1 Initialization

An object being "out of scene" actually refers to two scenarios: out of image boundary or too small to be recognized. Without loss of generation, this corresponds to both two cases when objects enter and exit the scene, as an example given in Figure 20. These two cases may be problematic for tracker initialization and termination if not handled correctly. An object may either be initialized when being partially visible or too small to be recognized. Different from the standard object tracking framework, tracking task in real-world use usually relies on external algorithms to find object candidates. Consequently, it is a critical step to the overall performance of any related surveillance task. In the following, we show how we apply the scene semantic knowledge into the tracking process and deal with the two scenarios above with a uniform affinity measurement.

In the computer vision field, for a rigid object, it is widely accepted to use a rectangle as the representation of an object: $\mathbf{r} = [\mathsf{x}, \mathsf{y}, w, \mathsf{h}]$, where $\mathbf{p}_\mathbf{r} = (\mathsf{x}, \mathsf{y})$ is the coordinates of the center point and (w, h) is the width and height. A straight line through point $\mathbf{p}$, parallel to vector $\boldsymbol{\nu}$ is define as $\mathsf{L}(\mathbf{p}, \boldsymbol{\nu})$. Similarly, a ray from point $\mathbf{p}$ in the direction of vector $\boldsymbol{\nu}$ is define as $\mathsf{R}(\mathbf{p}, \boldsymbol{\nu})$. For a rectangle $\mathbf{r}$ with a center point $\mathbf{p}_\mathbf{r}$, given its moving direction $\boldsymbol{\nu}_\mathbf{r}$, we have the following terms for the rectangle, also visually illustrated in Figure 21a and Figure 21b:

- *Perpendicular width:* the distance between two intersection points of line $\mathsf{L}(\mathbf{p}_\mathbf{r}, \boldsymbol{\nu}_{\mathbf{r}\cdot\text{perp}})$ and the rectangle $\mathbf{r}$, written as $W(\mathbf{r}, \boldsymbol{\nu}_\mathbf{r})$.
- *Last point:* the intersection point of ray $\mathsf{R}(\mathbf{p}_\mathbf{r}, -\boldsymbol{\nu}_\mathbf{r})$ with the rectangle $\mathbf{r}$, written as $\mathsf{P}(\mathbf{r}, \boldsymbol{\nu}_\mathbf{r})$.

Here $\boldsymbol{\nu}_{\mathbf{r}\text{perp}}$ is the vector perpendicular to $\boldsymbol{\nu}_\mathbf{r}$, such that $\boldsymbol{\nu}_\mathbf{r} \cdot \boldsymbol{\nu}_{\mathbf{r}\text{perp}} = 0$. Since the object's aspect ratio may vary with the object type and view point of the camera, by defining the *perpendicular width*, both width and height are taken into account. As we will show in the following, the definition of *last point* has a better interpretation of object's moving process, specifically for entering and exiting the scene.

In real-world applications, with no pre-determined object initialization available, applications usually rely on methods such as background subtraction and object detector, which usually tend to be error-prone. With the learned semantic knowledge, we only initialize objects that are around the entry area of the current available topics, with consistent direction and reasonable size. Consequently, noisy candidates with inconsistent motions or far away from the entry area will be effectively eliminated.

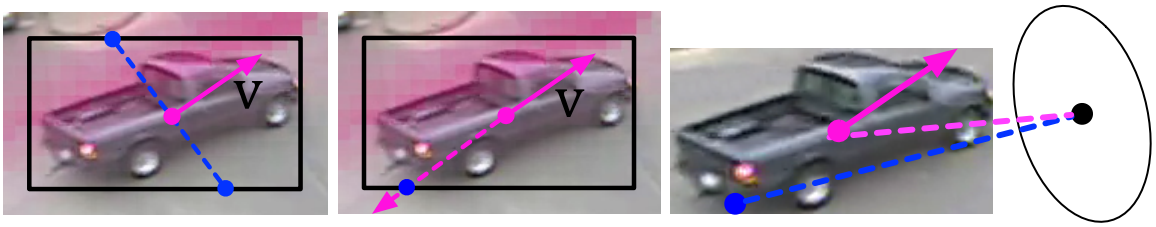

(a) (b) (c)

Figure 21: All the solid pink arrows above indicate the moving direction $\boldsymbol{\nu}_{\mathbf{r}}$, the pink dot is the center of the rectangle, blue dots are the intersection points with the rectangle. a: perpendicular width $W(\mathbf{r}, \boldsymbol{\nu}_{\mathbf{r}})$ of the object's bounding box wrt. to direction $\boldsymbol{\nu}_{\mathrm{r}}$, shown as the blue dash line. b: last point $\mathsf{P}(\mathbf{r}, \boldsymbol{\nu}_{\mathbf{r}})$ of the object's bounding box $\mathbf{r}$, where the dash arrow is $\mathsf{R}(\mathbf{r}, -\boldsymbol{\nu}_{\mathbf{r}})$. c: distance between a hotspot with a rectangle's center point and last point $\mathsf{P}(\mathbf{r}, \boldsymbol{\nu}_{\mathbf{r}})$, shown in pink and blue dash lines.

To quantitatively represent the affinity of an object to a topic k's entry area, we define the following metric:

$$\begin{aligned} \mathsf{S}_{\text{entry}}(\mathbf{r}, \mathsf{k}) = \frac{1}{3} \times \Big[& \Big(1 - \frac{\mathsf{D}(\mathsf{P}(\mathbf{r}, \boldsymbol{\nu}_{\mathbf{r}}), \mathbf{p}_{\mathsf{k}}(\text{entry}))}{\mathsf{D}(\mathbf{p}_{\mathsf{k}}(\text{entry}), \mathbf{p}_{\mathsf{k}}(\text{exit}))}\Big) \\ & + \left(1 - \frac{|W(\mathbf{r}, \boldsymbol{\nu}_{\mathbf{r}}) - W_{\mathsf{k}}(\mathbf{p}_{\mathbf{r}})|}{W(\mathbf{r}, \boldsymbol{\nu}_{\mathbf{r}}) + W_{\mathsf{k}}(\mathbf{p}_{\mathbf{r}})}\right) \\ & + \cos\left(\boldsymbol{\nu}_{\mathbf{r}}, \boldsymbol{\nu}_{\mathsf{k}}(\text{entry})\right) \Big] \end{aligned} \tag{4.1}$$

Here $\mathsf{D}(\cdot)$ is the distance measurement of two arbitrary points, we simply use Euclidean distance here. $\mathbf{p}_{\mathsf{k}}(\text{entry})$ and $\mathbf{p}_{\mathsf{k}}(\text{exit})$ are the entry and exit point of topic k, where the entry/exit points are the Gaussian mean obtained in §3.3.3. $W_{\mathsf{k}}(\mathbf{p}_{\mathbf{r}})$ and $\boldsymbol{\nu}_{\mathsf{k}}(\mathbf{p}_{\mathbf{r}})$ are the perpendicular width and main direction of topic k at location $\mathbf{p}_{\mathrm{r}}$.

The first term in the square parenthesis is the distance of $P(\mathbf{r}, \boldsymbol{\nu}_\mathbf{r})$ to the exit point, relative to the entry point. It produces a high value for bounding boxes around the entry area, taking the extent of the topic into account without placing any hard threshold. Note that instead of using the center of the rectangle $\mathbf{p}_r$, we use the last point of it. As illustrated in Figure 21c, when computing the distance of the object's bounding box and the hotspot, with the moving direction available, considering the last point along the direction measures the movement of the entire object. In other words, despite various object size, by ensuring the last point close to the entry/exit area, the entering/exiting process completes for the entire object. The second term will be close to 1 if and only if $W(\mathbf{r}, \boldsymbol{\nu}_\mathbf{r})$ and $W_k(\mathbf{p}_\mathbf{r})$ are similar. This penalizes bounding boxes of size either too large or too small, making sure the qualified candidate has a reasonable size relative to the topic's perpendicular width.

To deal with objects close to the image boundary, we do not initialize a tracker until the last point of the bounding box $\mathbf{r}$ is apart from the image boundary at least a margin distance; for an object enters with a tiny size, initialization is not considered when the object movement $\|\boldsymbol{\nu}_\mathbf{r}\|_2$ equals 0, since tiny size usually indicates tiny movement. Satisfying the above two cases, we initialize an object with a bounding box $\mathbf{r}$ once $S_{\text{entry}}(\mathbf{r}, k) > \sigma_1$ for a certain k.

4.3.2 Termination

When the tracked object manages to reach the exit area, it is quite likely to be well tracked, due to our checking scheme described later in §4.3.3. Therefore, we consider terminating a

tracker once it is close to its topic's exit area. Similarly, we define a distance measurement of a rectangle $\mathbf{r}$ with its exit area:

$$S_{\text{exit}}(\mathbf{r}, k) = 1 - \frac{D\left(P(\mathbf{r}, \boldsymbol{\nu}_{\mathbf{r}}), \mathbf{p}_k(\text{exit})\right)}{D\left(\mathbf{p}_k(\text{entry}), \mathbf{p}_k(\text{exit})\right)} \tag{4.2}$$

where we think the object passes through its exit area when $S_{\text{exit}}(\mathbf{r}, k) > \sigma_2$. However, in case the object is still able to be correctly tracked, we mark it and keep tracking until it gets lost, we call this phase *extended tracking*. The final trajectory is until the object gets lost. This is especially useful when the object exists with a tiny size. Due to the filtering of the topic model training process, tiny movements are filtered as noises. However, when the object can be tracked beyond the exit zone, it is better to keep a longer trajectory.

4.3.3 Tracking quality evaluation

An object's size, location, and motion are well constrained once we have a topic assignment of it. Once we initialize a tracker, we check the tracking quality on every frame. In general, we want objects to move smoothly and follow its visual topic. To quantitatively evaluate this, we define a smoothness term for an object's scale change:

$$S(\mathbf{r}_1, \mathbf{r}_2) = \frac{1}{2}\left[\left(1 - \frac{|w_1 - w_2|}{w_1 + w_2}\right) + \left(1 - \frac{|h_1 - h_2|}{h_1 + h_2}\right)\right], \tag{4.3}$$

here w_i and h_i are the width and height of rectangle $\mathbf{r}_i$, separately. $S(\mathbf{r}_1, \mathbf{r}_2)$ makes sure there is no abrupt scale change between two consecutive frames. Besides that, to evaluate how well the object is tracked, we have to consider regular tracking and extended tracking differently.

Before the object reaches its exit area, it is supposed to follow the corresponding visual topic tightly, possibly with occasional stops. So the tracking score is defined as:

$$S_{\text{track}}(\mathbf{r}, k, t) = \frac{1}{3}\Big[\Big(1 - \frac{|W(\mathbf{r}_t, \boldsymbol{\nu}_{\mathbf{r}_t}) - W_k(\mathbf{p}_{\mathbf{r}_t})|}{W(\mathbf{r}_t, \boldsymbol{\nu}_{\mathbf{r}_t}) + W_k(\mathbf{p}_{\mathbf{r}_t})}\Big) + S(\mathbf{r}_t, \mathbf{r}_{t-1}) + \cos(\boldsymbol{\nu}_{\mathbf{r}_t}, \boldsymbol{\nu}_k(\mathbf{p}_{\mathbf{r}_t}))\Big] \tag{4.4}$$

However, once the object passes through its exit area, it is expected to be terminated once it is not well tracked. Additionally, zero movements are not allowed. Since the object is not likely to pass through high-density grids in extended tracking phase, we compare the object's moving direction with the exit direction. A similar measurement is defined as:

$$S_{\text{extend}}(\mathbf{r}, k, t) = \frac{1}{2}\left[S(\mathbf{r}_t, \mathbf{r}_{t-1}) + \cos(\boldsymbol{\nu}_{\mathbf{r}}, \boldsymbol{\nu}_k(\text{exit}))\right] \tag{4.5}$$

In both measurement above, the notations are all similar with before, except that a subscript t is added, indicating the corresponding variable at frame t. $\boldsymbol{\nu}_k(\mathbf{p}_{\mathbf{r}_t})$ and $\boldsymbol{\nu}_k(\text{exit})$ are the main direction of topic k at $\mathbf{r}_t$'s center point $\mathbf{p}_{\mathbf{r}_t}$, and exit area. A valid tracking is defined as $S_{\text{track}}(\mathbf{r}, k, t) > \sigma_3$ or $S_{\text{extend}}(\mathbf{r}, k, t) > \sigma_4$, depending on whether it has passed through its exit area. Unqualified tracking will be discarded as failures along the way. By checking the tracking quality in this way, it is guaranteed that objects manage to pass the exit area follows its topic well and has a smooth movement and scale change. Empirically, $\sigma_1 \sim \sigma_4$ between $0.7 \sim 0.8$ are a reasonable threshold.

4.4 Semantic tracker

4.4.1 Semantic knowledge update

With some successfully tracked objects, we may adaptively update the semantic scene. More specifically, we update the corresponding topics with well-tracked objects, which are those enter through the entry area, tightly follow its belonging topic, and successfully exit through exit areas. The scene is updated as follows: The first and last location, along with the direction of a high-quality trajectory is used to update the entry/exit candidates; the rectangle perpendicular width wrt. its topic is used to update the topic perpendicular within its extent, where the updated value remains the mean of all the updates. By such iterative updating, we have more representative scene knowledge regarded to object tracking. The entry/exit area may gradually shift to where most objects enter and exit, where the perpendicular width of each topic also better fits the object statistics. The entire process is described in Algorithm 4 to 6.

4.5 Evaluation

4.5.1 Tracking accuracy

The extracted movements and entry/exit locations are hard to evaluate quantitatively, due to a lack of both ground-truth and accepted difference metrics. Instead, we extend a vehicle tracker with initialization- and update filters based on movements and entry/exit locations extracted from the scene, as described in the previous section.

Figure 22 shows our main result. Here, we compare the tracker from (9), labeled *heuristic*, against our version extended with a scene learning filter, labeled *scene*. Although the *heuristic* tracker relies on several manually tuned parameters, this is one of the few benchmarks that

Algorithm 4 Tracking with semantic knowledge.

for each frame t **do**
  Topic model inference on the frame.
  Obtain foreground boxes $\mathbf{R}_{bg} = \{\mathbf{r}_{bg}\}$.
  Obtain detection boxes $\mathbf{R}_{det} = \{\mathbf{r}_{det}\}$.
  for each i th object O_i at $\mathbf{r}_{t-1}(i)$, $(i = 1, \ldots, N_t)$ **do**
    Get topic assignment $k_t(i)$.
    Find the most matched boxes $\mathbf{r}_{bg}(i)$ and $\mathbf{r}_{det}(i)$ with $\mathbf{r}_{t-1}(i)$.
    $\mathbf{R}_{bg} = \mathbf{R}_{bg} \setminus \mathbf{r}_{bg}(i), \mathbf{R}_{det} = \mathbf{R}_{det} \setminus \mathbf{r}_{det}(i)$.
    Compute mean velocity $\boldsymbol{\nu}(i)$ within $\mathbf{r}_{t-1}(i)$ from the optical flow.
    Make measurement for tracking update $\boldsymbol{z}_t(i) = [\mathbf{r}_{bg}(i), \mathbf{r}_{det}(i), \boldsymbol{\nu}(i)]$.
    Set measurement covariance error R.
    Update object tracker with $\boldsymbol{z}_t(i)$ and R, get result $\mathbf{r}_t(i)$.
    CheckExitSemantic$(O_i, \mathbf{r}_t(i), k_t(i), t)$
  for Each remaining box candidate $r \in \{\mathbf{R}_{bg} \bigcup \mathbf{R}_{det}\}$ **do**
    CheckEntrySemantic$(\mathbf{r})$.

Algorithm 5 CheckExitSemantic$(O, \mathbf{r}, k, t)$

if O is in extended tracking phase **then**
  if $S_{extend}(\mathbf{r}, k, t) <= \sigma_4$ **then**
    Exit object.
else if $S_{track}(\mathbf{r}, k, t) < \sigma_3$ **then**
  Discard object.
if $S_{exit}(\mathbf{r}, k) > \sigma_2$ **then**
  Enter extended tracking phase.

Algorithm 6 CheckEntrySemantic$(\mathbf{r})$

Get the topic k for $\mathbf{r}$ at this frame.
if $S_{entry}(\mathbf{r}, k) > \sigma_1$ **then**
  Initialize object.

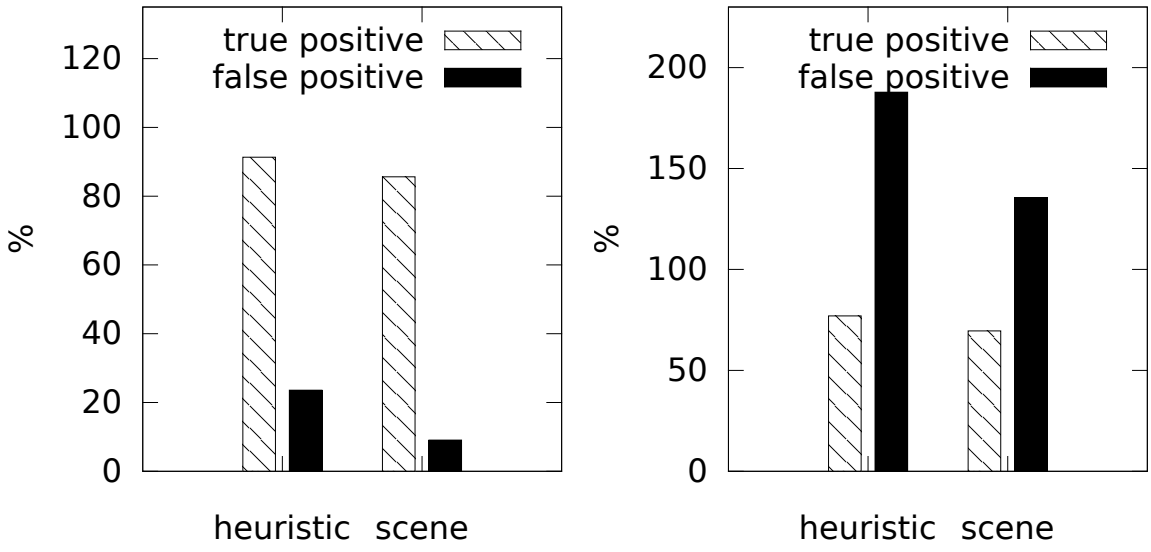

(a) Low resolution videos. (b) High resolution videos.

Figure 22: The number of true positive and false positve trackers. The black lines mark the ground truth, the striped and black bar are the true positive and false positive, separately.

quantitatively evaluate tracking including initialization and termination, which is critical for any realistic vehicle tracking application.

Here, true and false positives are based on matching tracked vehicles with ground truth trajectories. We use the *overlap* of two rectangles, defined by the intersection over union for a rectangle box $\mathbf{r}$ and a ground truth $\mathbf{r}_0$,

$$\text{Overlap}(\mathbf{r}, \mathbf{r}_0) = \frac{\text{A}(\mathbf{r} \cap \mathbf{r}_0)}{\text{A}(\mathbf{r} \cup \mathbf{r}_0)},$$

averaged over the frames in which the ground truth trajectory or the tracking result occurs.

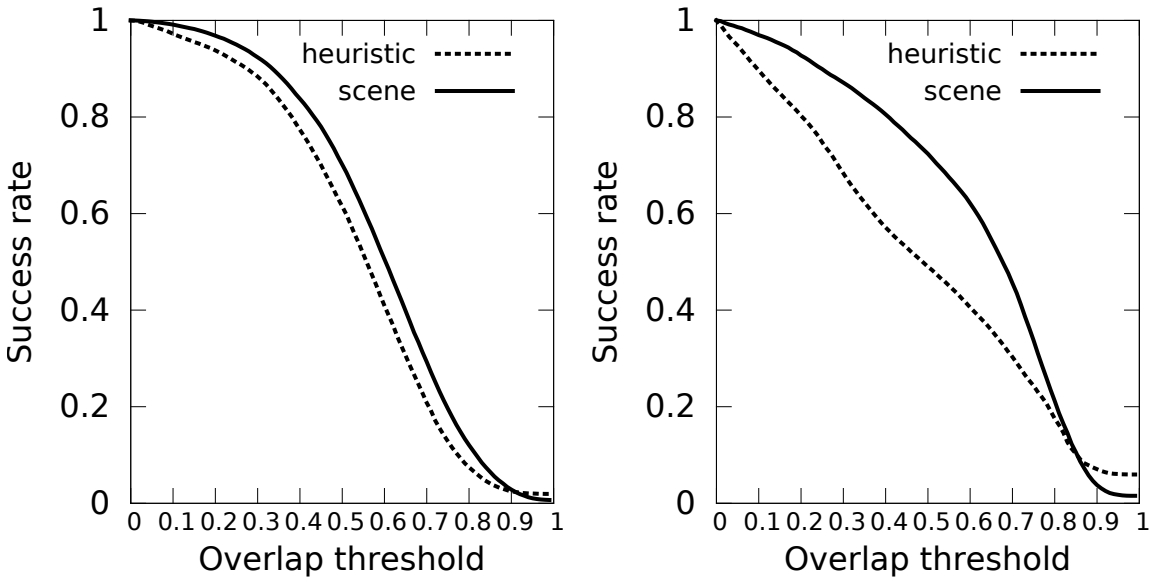

(a) Low resolution videos. (b) High resolution videos.

Figure 23: Success rate plot.

As in (9), we match each ground truth trajectory to the tracking result with the greatest overlap and use overlap > 0.3 to indicate a true positive. Any ground truth trajectories without a true positive match are considered false negatives, and any tracking result without a matched ground-truth trajectory with overlap ¿ 0.3 is considered a false positive. We find that our scene learning filter dramatically reduces false positives while keeping true positives essentially constant.

A large number of false positives remain for the high-resolution videos. Due to the complex vehicle interactions in high the resolution video (see Figure 19), even with the semantic knowledge, the naïve Kalman Filter may easily lose track, resulting in an increased false positive count.

Figure 23 shows the success plot of the two trackers for both simple and complex videos. Here, the *success rate* is defined as the fraction ground-truth trajectories that have a minimum overlap with its matched tracking output. Thus, the success rate measures how closely the matched trajectories actually match the ground truth. The larger area under the curves is, the better the tracking is. We see significant improvement in tracking accuracy with the help of scene learning, especially on the more complex videos.

In conclusion, we find that filtering tracker initialization and update using scene learning can significantly improve tracker performance, both in terms of precision and accuracy.

4.6 Related work

To ensure the accuracy for practical use, most surveillance system heuristically relies on prior knowledge, such as a specific deployment of the cameras or human input. For example, by calibration with know camera specifications, (52; 53) restores the real-world coordinates and infers the actual measurement of the tracked objects. Another type of work requires the area of interest for the tracked objects in advance, such as entry/exit area in (49; 50; 51), and a skeleton of the road surface in (54). None of the above methods is easy to apply to new camera settings.

To understand the scene in the videos, current work either learns the semantic areas or movement patterns. The former such as (43; 55; 56) learn the entry/exit areas from the trajectories already available or on-the-fly. Such methods require robust trajectories, which may not always be available in practical use. On the contrary, the latter (45; 47; 57; 58) statistically

learn the motions from the quantized optical flow, without knowledge of the actual objects in the scene, therefore, are more robust and flexible.

On the other hand, some researchers are working on the semantic aided tracking. (59; 60) use motion information to constrain the movement of the tracked objects; however, they are only for crowded scenes, since single object-trackers prefer appearance-based features. There are also work exploring scene evidence from trajectories: either from existing trajectories (61) or hand-drawn artificial trajectories (62). However, reliable trajectories still remain an issue for real-world application.

Despite the robust results in Bayesian motion learning, little work has extended them to vehicle tracking. Zhao etc. (48) applies (45) to vehicle counting. However, we still lack a general component for automatic initialization/termination to fit in the current tracking framework.

CHAPTER 5

SCENE-SPECIFIC MOTION MODEL

5.1 Introduction

The underlying assumption in §2.3 is that vehicles follow the constant acceleration model in a short period, like in the physical world. However, everything the scene experiences distortion under projection in most traffic videos. Therefore, vehicles' movement does not follow the linear model in Equation 2.1, and a linear state model is insufficient for the Kalman Filter to capture the movement pattern of the vehicles in the scene.

When good observations are available consistently, the Kalman filter can follow the tracked vehicle, even though the linear model cannot accurately reflect the size and velocity change. With missing observation or occlusion, the tracker is expected to predict with its internal model in the *extrapolation* mode. However, with the linear model broken, the tracker can only generate reasonable results for a short period.

To tackle this problem, we proposed a Unscented Kalman Filter (UKF) tracker, which learns a non-linear model from the history trajectories by Gaussian Process (GP). The semantic knowledge is the prerequisite of the non-linear model, which ensures the trajectories of high quality. Under the constraints of semantic learning, every vehicle that survives to the exit hotspot is consistent with its motion topic in terms of entry/exit location, size, and velocity.

5.2 Gaussian Process

Gaussian Process is a non-parametric model that learns a distribution over functions $f \sim \mathcal{GP}$. Given a dataset $\mathcal{D} = \{(\mathbf{x}_i, y_i), \mathbf{x}_i \in \mathbb{R}^d, y \in \mathbb{R}, i = 1, \ldots, N\}$, where $y_i = f(\mathbf{x}_i)$, a GP assumes a prior distribution that $f(\mathbf{x}_1), f(\mathbf{x}_2), \ldots, f(\mathbf{x}_N)$ jointly follows a Gaussian distribution $p(\mathbf{f}|\mathbf{X}) = \mathcal{N}(\mathbf{f}|\mu, \mathbf{K})$ where $\mathbf{K}_{ij}$ is defined by a kernel function $\mathbf{K}_{ij} = \kappa(\mathbf{x}_i, \mathbf{x}_j)$. When N_* new data points come, by the definition of GP, the joint distribution is still a Gaussian distribution

$$\begin{pmatrix} \mathbf{y} \\ \mathbf{f}_* \end{pmatrix} \sim \mathcal{N}\left(\begin{pmatrix} \mu \\ \mu_* \end{pmatrix}, \begin{pmatrix} \mathbf{K} & \mathbf{K}_* \\ \mathbf{K^T}_* & \mathbf{K}_{**} \end{pmatrix}\right), \tag{5.1}$$

where $\mathbf{K} = \kappa(\mathbf{X}, \mathbf{X})$ is $N \times N$, $\mathbf{K}_* = \kappa(\mathbf{X}, \mathbf{X}_*)$ is $N \times N*$, and $\mathbf{K}_{**} = \kappa(\mathbf{X}_*, \mathbf{X}_*)$ is $N_* \times N_*$.

By the conditioning Gaussian (63), the posterior is $p(\mathbf{f}_*|\mathbf{X}, \mathbf{X}_*, \mathbf{y}) = \mathcal{N}(\mathbf{f}_*|\mu_*, \Sigma_*)$, where

$$\mu_* = \mu(\mathbf{X}_*) + \mathbf{K}_*^T \mathbf{K}^{-1}(\mathbf{y} - \mu(\mathbf{X})) \tag{5.2}$$

$$\Sigma_* = \mathbf{K}_{**} - \mathbf{K}_*^{\mathbf{T}} \mathbf{K}^{-\mathbf{1}} \mathbf{K}_* \tag{5.3}$$

For the regression task, we can use μ_* for the prediction. Usually we assume $\mu(\mathbf{X}) = 0, \mu(\mathbf{X})_* = 0$. The Radial Basis Function (RBF) kernel is used here

$$\kappa(\mathbf{x}_i, \mathbf{x}_j) = \sigma_f^2 \exp\left(-\frac{1}{2l^2}(\mathbf{x}_i - \mathbf{x}_j)^2\right), \tag{5.4}$$

where σ_f and l are hyper parameters of the GP.

5.2.1 Multiple output Gaussian Process

In our case, ideally, we want to learn a scene-specific motion model, which is a mapping of vehicle states between two consecutive frames. The history trajectories provide such mapping for training. Different with §2.3, each data point $\mathbf{x}$ is the internal state $[x, y, w, h, x', y']$, representing the location, size and velocity of vehicle. Each dimension of the output $\mathbf{y}$ exactly matches the input since it is the input for the next time step. In §5.2, y is a real value, while here it is extended to multiple output GP, where $\mathbf{y} \in \mathbb{R}^4$. Despite the different output dimension, the GP is trained jointly over all the dimensions and the prediction for regression is the same with Equation 5.3, equivalent to the case that each dimension of the output is independent.

5.2.2 Online processing for streaming data

5.3 Unscented Kalman Filter

In Kalman Filter, there are two important models,

- Internal state model: $\mathbf{x}_t = f(\mathbf{x}_{t-1}, \mathbf{w}_{t-1})$
- Observation model: $\mathbf{z}_t = h(\mathbf{x}_t, \mathbf{v}_t)$

where $\mathbf{x}_t$ and $\mathbf{z}_t$ are the internal state and the observation, $\mathbf{w}_t$ and $\mathbf{v}_t$ are the process and measurement noise at time t, and both $f(\cdot)$ and $h(\cdot)$ are assumed linear. However, in many cases, at least one of the linear models does not hold. Therefore, methods for Kalman Filter with nonlinear model are proposed, including Extended Kalman Filter (EKF) (64) and UKF (65). EKF uses Taylor series expansion to approximate the nonlinearity, may introduce errors for the true mean and covariance of the state variables after the non-linear transformation. Additionally, in our case, there is no close-formed nonlinear motion model under camera pro-

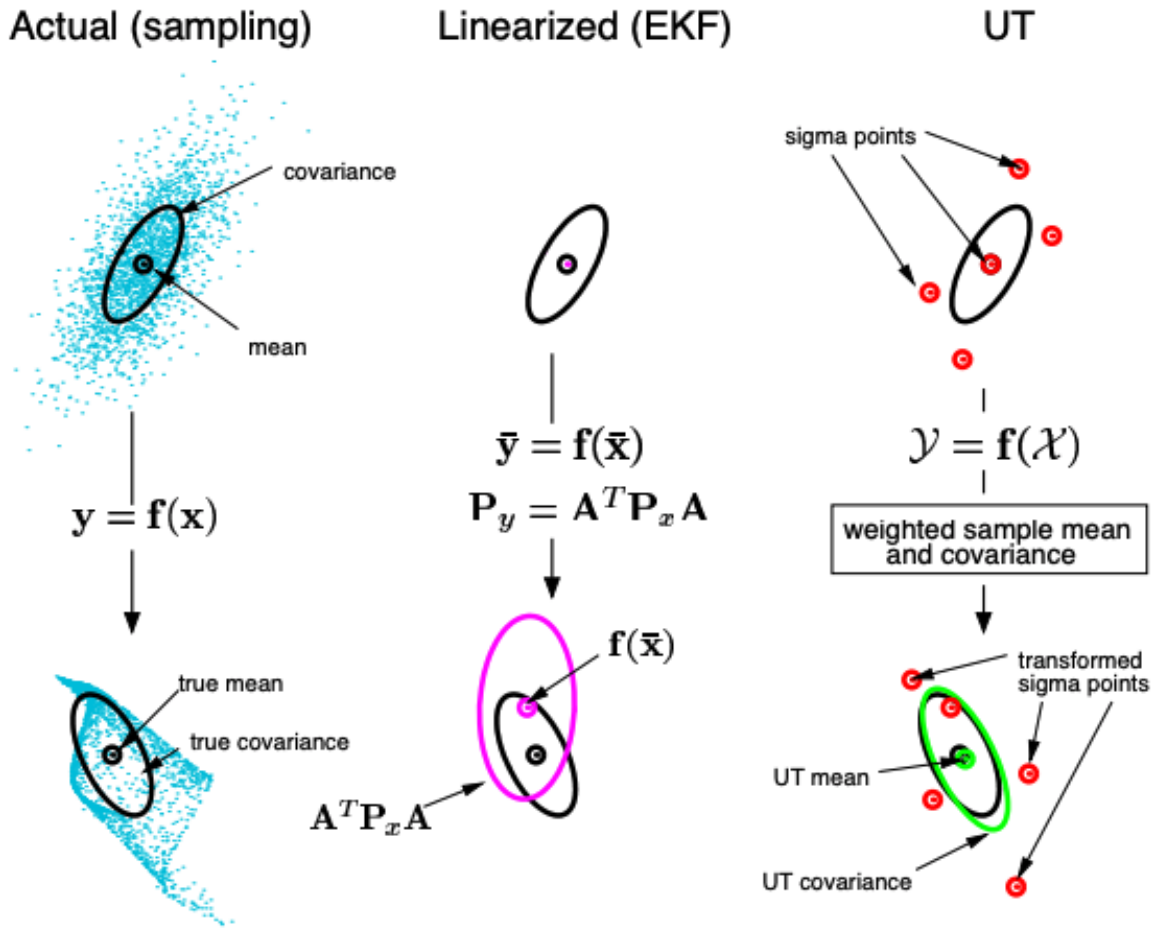

Figure 24: Example of the UT for mean and covariance propagation. a) actual, b) first-order linearization (EKF), c) UT.

jection. Consequently, we use UKF, where its nonlinear state model $\mathsf{f}(\cdot)$ is learned by the non-parametric model GP.

The key of UKF is unscented transformation (UT), which calculates the statistics of random variables under a nonlinear transformation, accurately capturing the mean and the covariance to the 3rd order Taylor series expansion for Gaussian inputs. For a random variable $\mathbf{x} \in \mathbb{R}^{\mathrm{d}}$

with mean $\bar{\mathbf{x}}$ and covariance $\mathbf{P}_{\mathbf{x}}$, to calculate the statistics of $\mathbf{z}$ under a nonlinear mapping $\mathbf{z} = g(\mathbf{x})$, first a set of sigma points are built around the $\bar{\mathbf{x}}$ (65),

$$\begin{aligned}
\mathcal{X}_0 &= \bar{\mathbf{x}} \\
\mathcal{X}_i &= \bar{\mathbf{x}} + (\sqrt{(d+\lambda)\mathbf{P}_{\mathbf{x}}})_i, \qquad i = 1, \ldots, d \\
\mathcal{X}_i &= \bar{\mathbf{x}} - (\sqrt{(d+\lambda)\mathbf{P}_{\mathbf{x}}})_i, \qquad i = d+1, \ldots, 2d \\
W_0^{(m)} &= \lambda/(d+\lambda) \\
W_0^{(c)} &= \lambda/(d+\lambda) + (1 - \alpha^2 + \beta) \\
W_i^{(m)} &= W_i^{(c)} = 1/\{2(d+\lambda)\} \qquad i = 1, \ldots, 2d
\end{aligned} \tag{5.5}$$

where α controls the spread of the sigma points around $\bar{\mathbf{x}}$, $\lambda = \alpha^2(d+\kappa) - d$ and κ are the scaling parameters, β describe the prior knowledge for the distribution of $\mathbf{x}$. α is usually set to a small value (*e.g.*$1e-3$), κ is usually set to 0 and β is optimally set to 2 for Gaussian distribution. $(\sqrt{(d+\lambda)\mathbf{P}_{\mathbf{x}}})_i$ is the ith row of the matrix square root. Each sigma point is propagated through the nonlinear function $g(\cdot)$,

$$\mathcal{Z}_i = g(\mathcal{X}_i) \qquad i = 0, 1, \ldots, 2d,$$

The mean and covariance for $\mathbf{z}$ are approximated by the weighted sample mean and covariance of the posterior sigma points,

$$\bar{\mathbf{z}} \approx \sum_{i=0}^{2d} W_i^{(m)} \mathcal{Z}_i \tag{5.6}$$

$$\mathbf{P}_{\mathbf{z}} \approx \sum_{i=0}^{2d} W_i^{(c)} (\mathcal{Z}_i - \bar{\mathbf{z}})(\mathcal{Z}_i - \bar{\mathbf{z}})^T \tag{5.7}$$

Therefore, with the non-linear state and measurement model, UKF naturally extends the unscented transformation by applying it alternately between the predict and correct step.

5.4 GP-UKF tracker

In the tracking setting, the state model is a nonlinear GP model while the measurement model is still linear.

$$\mathbf{x}_t = f(\mathbf{x}_{t-1}) = GP(\mathbf{x_{t-1}}, \mathbf{X}) \tag{5.8}$$

$$\mathbf{z}_t = h(\mathbf{x}_t) = H\mathbf{x}_t, \tag{5.9}$$

Similar with §2.3, the observation is still the bounding boxes generated by background subtraction model and vehicle detector, and filtered pixel movement from optical flow:

$$\mathbf{z} = [x^{bg}, y^{bg}, w^{bg}, h^{bg}, x^{det}, y^{det}, w^{det}, h^{det}, v_x, v_y].$$

Similarly, the measurement model H is a 6×10 matrix with 1 at $(0,0)$, $(1,1)$, $(2,2)$, $(3,3)$, $(0,4)$, $(1,5)$, $(2,6)$, $(3,7)$, $(4,8)$, $(5,9)$.

Algorithm 7 GP-UKF.

Require: State transition mapping $\{\mathbf{x}_{t-1}, \mathbf{x}_t\}$ from history data.

1: Start with $\hat{\mathbf{x}}_0 = \mathbf{x}_0$.

2: Calculate the sigma points: $\mathcal{X}_{t-1} = \left[\hat{\mathbf{x}}_{t-1}, \hat{\mathbf{x}}_{t-1} \pm \sqrt{(d+\lambda)P_{t-1}}\right]$.

3: Predict:

$$\hat{\mathcal{X}}_{i,t} = \mathrm{GP}_\mu(\mathcal{X}_{i,t-1}, \mathbf{X}), \quad i = 0, \ldots, 2d$$

$$\hat{\mathbf{x}}_t^- = \sum_{i=0}^{2d} W_i^{(m)} \hat{\mathcal{X}}_{i,t}$$

4:

$$P_t^- = \sum_{i=0}^{2d} W_i^{(c)} [\hat{\mathcal{X}}_{i,t} - \hat{\mathbf{x}}_t^-][\hat{\mathcal{X}}_{i,t} - \hat{\mathbf{x}}_t^-]^T$$

$$\hat{\mathcal{Z}}_t = \left[H\hat{\mathcal{X}}_{i,t}\right], \quad i = 0, \ldots, 2d$$

$$\hat{\mathbf{z}}_t^- = \sum_{i=0}^{2d} W_i^{(m)} \hat{\mathcal{Z}}_{i,t}$$

5: Get measurement covariance of $\mathbf{z}_t$: $R_t = \mathrm{GP}_\sigma(\mathbf{z}_t, \mathbf{X})$.

6: Correct with measurement:

$$P_{\hat{\mathbf{z}}_t, \hat{\mathbf{z}}_t} = \sum_{i=0}^{2d} W_i^{(c)} [\hat{\mathcal{Z}}_{i,t} - \hat{\mathbf{z}}_t^-][\hat{\mathcal{Z}}_{i,t} - \hat{\mathbf{z}}_t^-]^T + R_t$$

7:

$$P_{\hat{\mathbf{x}}_t, \hat{\mathbf{z}}_t} = \sum_{i=0}^{2d} W_i^{(c)} [\hat{\mathcal{X}}_{i,t} - \hat{\mathbf{x}}_t^-][\hat{\mathcal{Z}}_{i,t} - \hat{\mathbf{z}}_t^-]^T$$

$$K = P_{\hat{\mathbf{x}}_t, \hat{\mathbf{z}}_t} P_{\hat{\mathbf{z}}_t, \hat{\mathbf{z}}_t}^{-1}$$

$$\hat{\mathbf{x}}_t = \hat{\mathbf{x}}_t^- + K(\mathbf{z}_t - \hat{\mathbf{z}}_t^-)$$

$$P_t = P_t^- - K P_{\hat{\mathbf{z}}_t, \hat{\mathbf{z}}_t} K^T$$

(a) Kalman filter with Linear model. (b) Kalman filter with non-linear model.

Figure 25: Tracking screenshots at frame 854, no trajectory for Gaussian Process.

5.5 Evaluation

Figure 25, Figure 26, Figure 27 shows the comparison of the Kalman filter with linear and non-linear model, which we call KF (left) and GP-UKF (right). Under projection, vehicles moving towards the right of the frame has an increasing rate of size and velocity. In Figure 25, tracking just started. GP-UKF tracker does not have any training data, which works similarly with the KF tracker. In Figure 26, GP-UKF has accumulated 1-2 trajectories, showing a slightly better coverage of the actual vehicle. Finally, when GP-UKF has 5-8 trajectories as the training data, GP-UFK adapts to the scale and velocity significantly better than linear KF tracker in Figure 27.

5.6 Future work

(a) Kalman filter with linear model. (b) Kalman filter with non-linear model.

Figure 26: Tracking screenshots at frame 914, 1-2 trajectories for Gaussian Process.

(a) Kalman filter with linear model. (b) Kalman filter with non-linear model.

Figure 27: Tracking screenshots at frame 989, 5-8 trajectories for Gaussian Process.

CHAPTER 6

DATASET

6.1 Introduction

In the field that has such a massive amount of video data like intelligence transportation, computer vision has become a primary tool for information retrieval from those videos.

Usually, an agent has access to a specific kind of camera and aim to develop a system to perform a particular task. Therefore, such systems are usually restricted to some specific camera views or settings and hard to migrate to other tasks. Moreover, due to a large amount of videos, there is usually little annotation due to the expensive labor cost. It is hard to carry out a quantitative evaluation for those systems.

On the other hand, there lacks a comprehensive and widely accepted video dataset in the academic community. Although challenges like VOT (66) and MOT (67) are widely used in the object tracking community, the given data are relatively in small scale and lack real-world interactions, compared with what is directly acquired from the surveillance camera. For example, the videos in VOT and MOT mostly have a few hundred frames, lasting no later than 1 minute; even though a few videos exceed 1000 frames, it is still too short compared with real-world data. Such a short sequence cannot raise enough attention to algorithm throughput. Despite the occlusion and consequent difficulties in the above dataset, those videos fail to address the critical challenges for surveillance tasks. Most surveillance cameras are mounted

at a high place with little view changes, while the above popular datasets do not contain videos with such overlooking views. Besides, objects tend to have intermittent stops and severe occlusion at intersections, which is also rarely available in the above datasets.

We release a comprehensive traffic video dataset with vehicle trajectory ground truth, containing various adversarial interactions. We aim to provide other researchers with real-world data and raise more attention in such problems.

6.2 Dataset

To the best of our knowledge, there exists no public traffic surveillance video dataset containing complex real world interactions and illumination variations. Existing vision datasets are either not applicable to our scenario with different viewpoint (driver's view) (68) or contain short clips with limited adversarial conditions, scale changes, and illumination variations (62; 7). Even in the largest dataset collected (7), only 15 out of 98 videos exceeds 1000 frames (33 seconds).

We collected 13 representative surveillance videos across our state, from the local department of transportation, and annotated these using VATIC (69). Each object has its location and extent annotated on every frame, which is used as our ground truth. The average length of each video is five minutes (around 9000 frames), sufficient to cover several traffic signal cycles with real-world vehicle interactions and movement patterns. We divide the videos into two groups: simple low resolution (lowRes) and complex high resolution (highRes). Figure 28 shows screen shots from this dataset, and Table I gives an overview of our dataset, where the

rightmost four columns indicate the number of videos reflecting various challenging aspects: occlusion, shadows, distortion and pedestrians.

TABLE I: Dataset overview. The second and the third columns show the resolution and object size range in pixels, followed by number of videos under each group. The rightmost four columns show the number of videos reflecting various challenging aspects (occlusion, shadow, distortion and pedestrian).

Group	Resolution	Object size	#	Occlusion	Shadow	Distortion	Pedestrian
lowRes	342×228	32–44,814	5	3	1	3	0
	320×240	48–25,284	2	2	1	2	0
highRes	720×576	84–255,106	4	3	0	0	1

(a) (b) (c) (d) (e) (f)

(g) (h) (i) (j) (k) (l)

Figure 28: Snapshots of videos in our dataset, with various resolution, viewpoint, illumination, vehicle size and interactions. In particular, (c) shows shadows; (f) and (g) show severe distortion by fish-eye camera. We group these videos by their characteristics: (a) - (g) are simple low resolution videos (lowRes), and (h) - (l) are complex high resolution videos (highRes).

CHAPTER 7

VEHICLE COUNTING SYSTEM

7.1 Introduction

People in civil engineering are devoted to building a better social environment. As one of its sub-discipline, traffic engineering focuses on efficient traffic flow. It aims to achieve safe and efficient movement of people and goods on existing transportation infrastructures. For example, by properly designing road geometry, the average travel time may be shortened; by modification of the traffic lights and signs, the crash rate at a specific location could decrease significantly.

To make the right decision, sufficient data should be acquired to support quantitative analysis. Under the theory of traffic engineering, the famous Lane flow equation (70) describes the relationship between traffic flow and speed:

$$Q = KV,$$

where Q is the number of vehicles per hour, V is the mean speed, K is the vehicle density, usually can be changed by the speed limit, signals on the ramp entrance.

In general, we want our facilities to have maximal flow capacity, and Q is the quantity of interest. Therefore, the traffic flow Q needs to be obtained to evaluate the changes reflected by the decision made to the infrastructures. Apart from the traditional heavy equipment,

increasing attention and efforts have been put on analyzing the existing surveillance videos. For example, IDOT maintains a huge database of videos recorded by traffic cameras across Illinois 24/7. People are hired to manually count the number of vehicles and generate a report for each one-hour video, which is expensive both in labor and time. To help facilitate the process, we build an end-to-end vehicle counting system on top of our fully automatic tracker. The system runs in real time, generates a similar report for each video. It significantly reduces the cost and time for this process.

In practice, the tracking and counting process requires immense computational resource; therefore, these tasks usually run on remote servers. To allow easy access to the data and results, we build additional GUI tools to provide the users interactive operation, such as video upload, result visualization, and report generation. With end-to-end workflow and interactive GUI interface, the system can be easily deployed in large scale.

7.2 Vehicle counter

After the tracking process finishes, the number of trajectories is regarded as vehicle counts. However, the current traffic statistics of IDOT contains specific vehicle counts in different directions. To match the format of the existing reports, not only we have to obtain the total number of vehicles, each vehicle has to be correctly classified to its corresponding motion. The accumulative counts of each motion are the desired results. Consequently, vehicle movements have to be available apart from the tracking results. With different tracking strategy, motions are obtained differently: with our heuristic tracker, we rely on human annotated input; however, with the semantic tracker, we learn the motion offline by unsupervised learning.

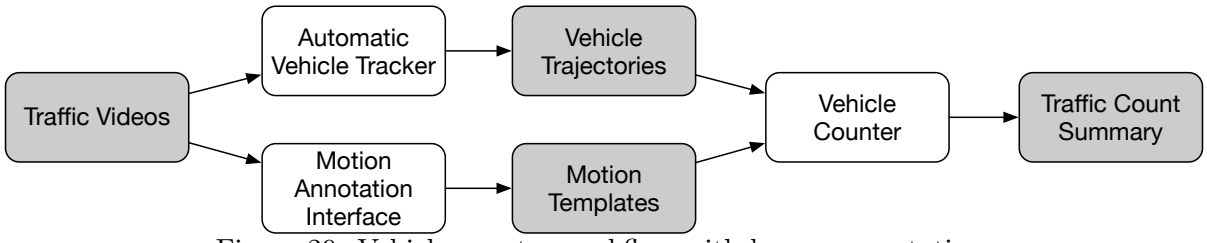

Figure 29: Vehicle counter workflow with human annotation.

7.2.1 Vehicle counter with human annotation

Initially, users upload videos via FTP and operated on our GUI interface by remote desktop. Our GUI interface and require the user to draw a few line segments as the templates of the vehicle motion, we call it *motion template*. Figure 30 is the screenshot of the interface, where the motion templates mostly align with the road surface. However, a road may have more than one motion due to potential multiple lanes. Figure 29 shows our first counter framework with the heuristic tracker. The tracker generates a set of vehicle trajectories; then each trajectory is assigned to a motion template that mostly matches its movement. By increasing the count of each vehicle's assigned motion template, we can obtain the final traffic count of each movement.

Suppose we have a set of n motion templates $\mathbf{T} = \{\mathbf{T}_1, \mathbf{T}_2, \ldots, \mathbf{T}_n\}$ and a set of trajectories of N vehicles $\Omega = \{\mathbf{O}_1, \mathbf{O}_2, \ldots, \mathbf{O}_N\}$.

7.2.2 Vehicle counter with semantic knowledge

Figure 31 shows the workflow of the improved counter with semantic knowledge. After offline learning in §3.2, the distribution of visual topics are learned; and each of them is a parameterized model. In the tracking process §4.2, the fitting of each tracked vehicle with

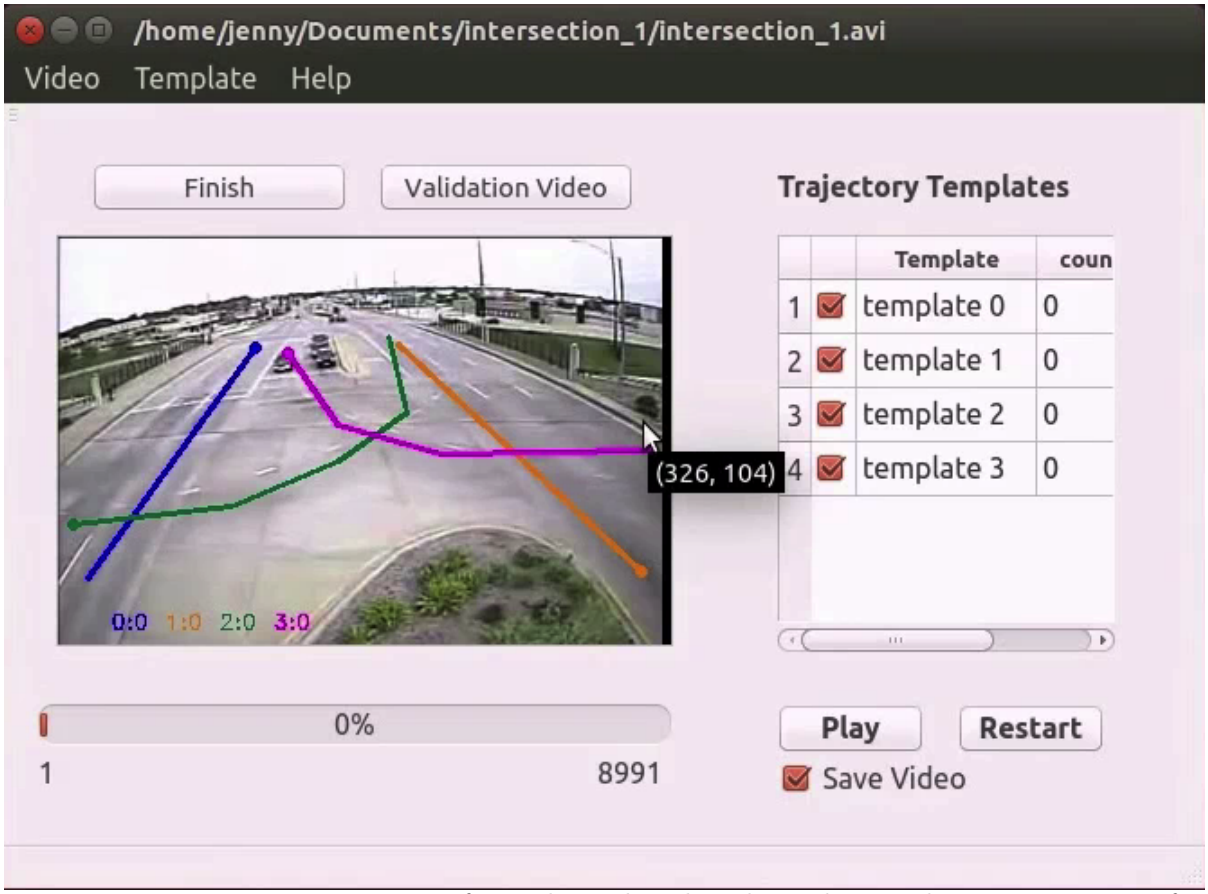

Figure 30: Motion annotation interface: the end with a dot indicates the starting point of a motion, the bottom of the image and the list on the right displays the counting results.

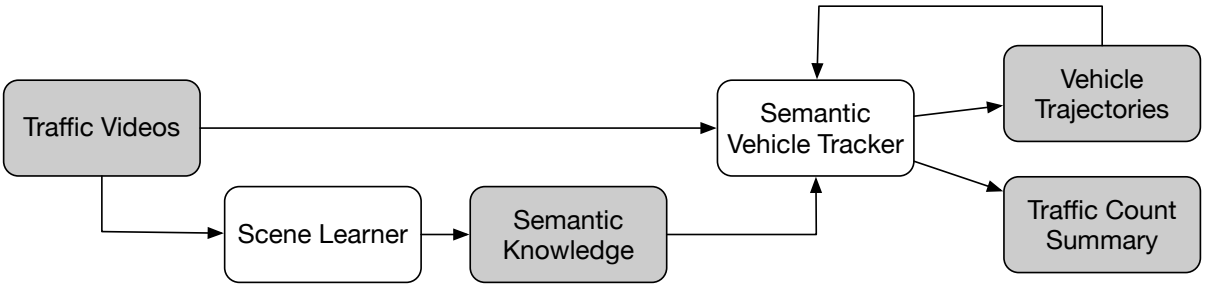

Figure 31: End-to-end vehicle counter workflow with scene understanding.

every model is examined by online inference. In other words, the motion of the tracked vehicle could be determined by the most fitted motion model. By increasing the vehicle count of each vehicle's motion upon leaving, counting could be done along with tracking.

7.2.3 Web portal

Based on the feedbacks from IDOT about our previous GUI interface, we build a web portal of this system that integrates all the previous functions. Currently, the system only supports manual template annotation as in Figure 29, the scene understanding module has not been integrated. Figure 32 is the main interface of camera display: cameras are displayed on the map, with a list of their name on the left. Users may create or browse cameras by list or on the map, and upload videos for each camera. Similar to our previous GUI, once a new camera is created and the first video is uploaded, the user needs to draw the motion templates. Then the tracker and counter are executed sequentially in the background. Users may return later to check the progress and download the results. We allow at most four videos processed at the same time. Figure 33 and Figure 34 are the interface for camera and videos. Each camera may

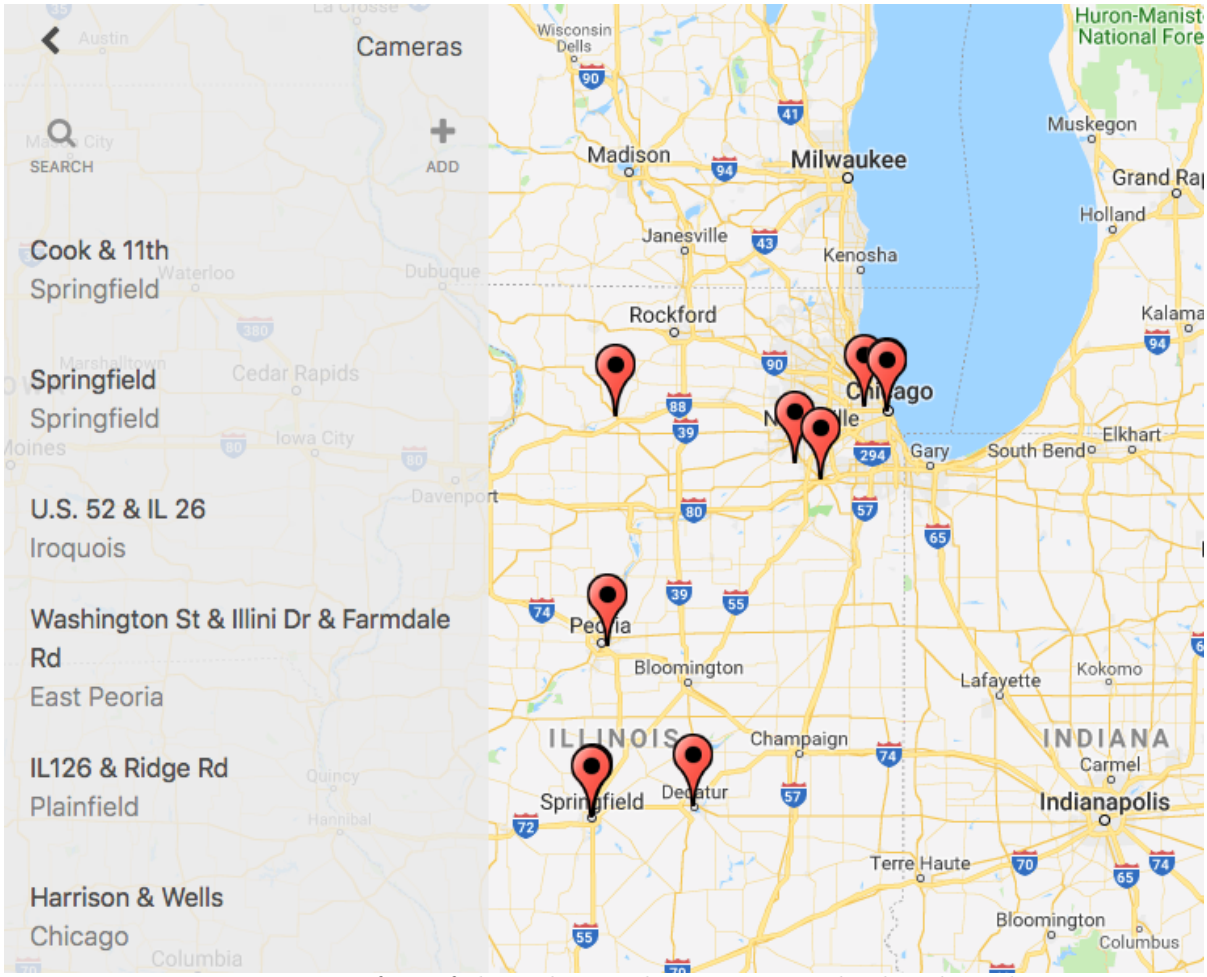

Figure 32: Main interface of the web portal, cameras are displayed on the map.

have multiple videos, all its videos, and their count summary is displayed on the left in the camera view. Clicking a video on the list leads to its individual video view. The video is played and detailed counts on each motion are displayed.

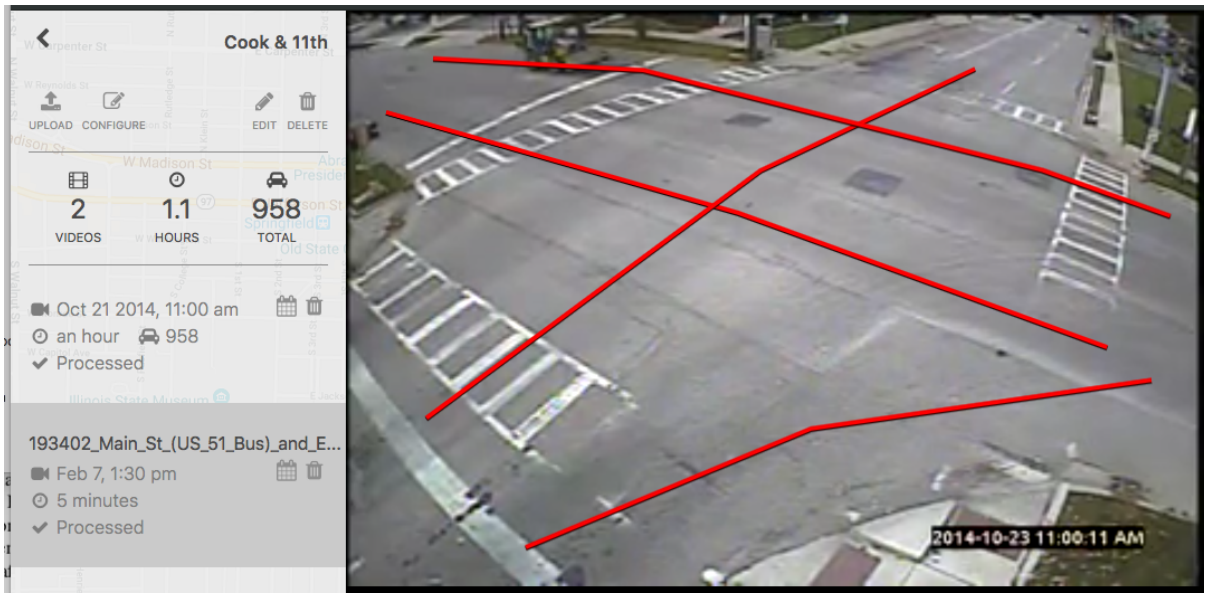

Figure 33: Camera view with video list and summary.

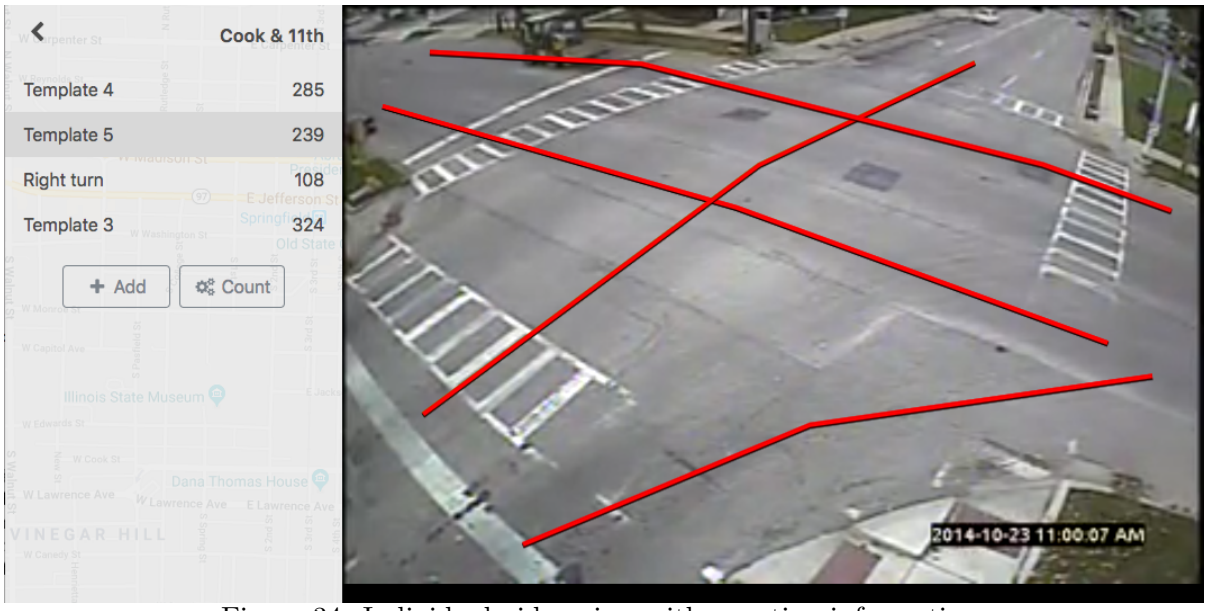

Figure 34: Individual video view with counting information.

CITED LITERATURE

1. Klein, L. A., Mills, M. K., and Gibson, D. R.: Traffic detector handbook: -volume ii. Technical report, 2006.

2. Mimbela, L. E. Y. and Klein, L. A.: Summary of vehicle detection and surveillance technologies used in intelligent transportation systems. 2000.

3. Dollar, P., Wojek, C., Schiele, B., and Perona, P.: Pedestrian detection: An evaluation of the state of the art. IEEE transactions on pattern analysis and machine intelligence, 34(4):743–761, 2012.

4. Parkhi, O. M., Vedaldi, A., Zisserman, A., et al.: Deep face recognition. In bmvc, volume 1, page 6, 2015.

5. Rautaray, S. S. and Agrawal, A.: Vision based hand gesture recognition for human computer interaction: a survey. Artificial intelligence review, 43(1):1–54, 2015.

6. Scime, L. and Beuth, J.: Anomaly detection and classification in a laser powder bed additive manufacturing process using a trained computer vision algorithm. Additive Manufacturing, 19:114–126, 2018.

7. Wu, Y., Lim, J., and Yang, M.-H.: Object tracking benchmark. IEEE Trans. on Patt. Anal. and Mach. Int., 37(9), 2015.

8. Seenouvong, N., Watchareeruetai, U., Nuthong, C., Khongsomboon, K., and Ohnishi, N.: A computer vision based vehicle detection and counting system. In 2016 8th International Conference on Knowledge and Smart Technology (KST), pages 224–227. IEEE, 2016.

9. Jin, Y. and Eriksson, J.: Fully automatic, real-time vehicle tracking for surveillance video. Computer and Robotic Vision, 2017.

10. Henriques, J. F., Caseiro, R., Martins, P., and Batista, J.: High-speed tracking with kernelized correlation filters. IEEE Trans. on Patt. Analysis and Mach. Int., 37(3):583–596, 2015.

11. Vojir, T., Noskova, J., and Matas, J.: Robust scale-adaptive mean-shift for tracking. Patt.Rec. Letters, 49:250–258, 2014.

12. Hare, S., Saffari, A., and Torr, P. H.: Struck: Structured output tracking with kernels. In ICCV, pages 263–270. IEEE, 2011.

13. Possegger, H., Mauthner, T., and Bischof, H.: In defense of color-based model-free tracking. In IEEE CVPR, pages 2113–2120, 2015.

14. Viola, P. and Jones, M.: Rapid object detection using a boosted cascade of simple features. In IEEE CVPR, volume 1, pages I–511. IEEE, 2001.

15. Dalal, N. and Triggs, B.: Histograms of oriented gradients for human detection. In CVPR, volume 1, pages 886–893. IEEE, 2005.

16. Felzenszwalb, P. F., Girshick, R. B., and McAllester, D.: Cascade object detection with deformable part models. In CVPR. IEEE, 2010.

17. Girshick, R., Donahue, J., Darrell, T., and Malik, J.: Rich feature hierarchies for accurate object detection and semantic segmentation. In IEEE CVPR, pages 580–587, 2014.

18. Barnich, O. and Van Droogenbroeck, M.: Vibe: A universal background subtraction algorithm for video sequences. Image Processing, IEEE Trans. on, 20(6):1709–1724, 2011.

19. Zivkovic, Z. and van der Heijden, F.: Efficient adaptive density estimation per image pixel for the task of background subtraction. Patt.Rec. letters, 27(7):773–780, 2006.

20. Ren, S., He, K., Girshick, R., and Sun, J.: Faster r-cnn: Towards real-time object detection with region proposal networks. In Adv. in neural info. processing systems, pages 91–99, 2015.

21. Lucas, B. D., Kanade, T., et al.: An iterative image registration technique with an application to stereo vision. In IJCAI, volume 81, 1981.

22. Grewal, M. S.: Kalman filtering. Springer, 2011.

23. Welch, G. and Bishop, G.: An introduction to the kalman filter. Technical report, Chapel Hill, NC, USA, 1995.

24. Kalal, Z., Mikolajczyk, K., and Matas, J.: Forward-backward error: Automatic detection of tracking failures. In Patt.Rec. (ICPR), 2010 20th Int. Conf. on. IEEE, 2010.

25. Wu, Y., Lim, J., and Yang, M.-H.: Online object tracking: A benchmark. In IEEE CVPR, June 2013.

26. Bertinetto, L., Valmadre, J., Golodetz, S., Miksik, O., and Torr, P. H.: Staple: Complementary learners for real-time tracking. In IEEE CVPR, pages 1401–1409, 2016.

27. Zhang, J., Ma, S., and Sclaroff, S.: Meem: robust tracking via multiple experts using entropy minimization. In European Conf. on Comp.Vis., pages 188–203. Springer, 2014.

28. Danelljan, M., Hager, G., Shahbaz Khan, F., and Felsberg, M.: Learning spatially regularized correlation filters for visual tracking. In IEEE Int. Conf. on Comp.Vis., pages 4310–4318, 2015.

29. Bernardin, K. and Stiefelhagen, R.: Evaluating multiple object tracking performance: the clear mot metrics. EURASIP Journal on Image and Video Processing, 2008(1):1–10, 2008.

30. Butt, A. A. and Collins, R. T.: Multi-target tracking by lagrangian relaxation to min-cost network flow. In IEEE CVPR., 2013.

31. Berclaz, J., Fleuret, F., Turetken, E., and Fua, P.: Multiple object tracking using k-shortest paths optimization. IEEE trans. on pattern analysis and machine intelligence, 33(9):1806–1819, 2011.

32. Kwon, J. and Lee, K. M.: Visual tracking decomposition. In CVPR, pages 1269–1276. IEEE, 2010.

33. Grabner, H., Grabner, M., and Bischof, H.: Real-time tracking via on-line boosting. In BMVC, volume 1, page 6, 2006.

34. Choi, W.: Near-online multi-target tracking with aggregated local flow descriptor. In IEEE ICCV, 2015.

35. Kalal, Z., Mikolajczyk, K., and Matas, J.: Tracking-learning-detection. IEEE trans. on patt. anal. and mach. int., 34(7), 2012.

36. Zhang, L., Li, Y., and Nevatia, R.: Global data assoc. for multi-object tracking using netw. flows. In CVPR'08, pages 1–8. IEEE, 2008.

37. Andriyenko, A. and Schindler, K.: Multi-target tracking by continuous energy minimization. In CVPR. IEEE, 2011.

38. Coifman, B., Beymer, D., McLauchlan, P., and Malik, J.: A real-time comp.vis. system for vehicle tracking and traffic surveillance. Transp. Res. Part C: Emerging Tech, 6(4):271–288, 1998.

39. Wang, W., Gee, T., Price, J., and Qi, H.: Real time multi-vehicle tracking and counting at intersections from a fisheye camera. In WACV, 2015.

40. Bulan, O., Loce, R. P., Wu, W., Wang, Y., Bernal, E. A., and Fan, Z.: Video-based real-time on-street parking occupancy detection system. J. of Electronic Imaging, 22(4):041109–041109, 2013.

41. Jiang, F., Yuan, J., Tsaftaris, S. A., and Katsaggelos, A. K.: Anomalous video event detection using spatiotemporal context. Comp.Vis. and Image Understanding, 115(3):323–333, 2011.

42. Chen, Y.-L., Wu, B.-F., Huang, H.-Y., and Fan, C.-J.: A real-time vision system for nighttime vehicle detection and traffic surveillance. IEEE Trans. on Indust. Elec., 58(5):2030–2044, 2011.

43. Tung, F., Zelek, J. S., and Clausi, D. A.: Goal-based trajectory analysis for unusual behaviour detection in intelligent surveillance. Image and Vision Computing, 29(4):230–240, 2011.

44. Xu, H., Zhou, Y., Lin, W., and Zha, H.: Unsupervised trajectory clustering via adaptive multi-kernel-based shrinkage. In Proceedings of the IEEE International Conference on Computer Vision, pages 4328–4336, 2015.

45. Wang, X., Ma, X., and Grimson, W. E. L.: Unsupervised activity perception in crowded and complicated scenes using hierarchical bayesian models. PAMI, 31(3):539–555, 2009.

46. Yee Whye, T., JORDAN, M. I., Matthew, J., and David, M.: Hierarchical dirichlet processes. 2006.

47. Kuettel, D., Breitenstein, M. D., Van Gool, L., and Ferrari, V.: What's going on? discovering spatio-temporal dependencies in dynamic scenes. In Computer Vision and Pattern Recognition (CVPR), 2010 IEEE Conference on, pages 1951–1958. IEEE, 2010.

48. Zhao, R. and Wang, X.: Counting vehicles from semantic regions. IEEE Transactions on Intelligent Transportation Systems, 14(2):1016–1022, 2013.

49. Tamersoy, B. and Aggarwal, J. K.: Robust vehicle detection for tracking in highway surveillance videos using unsupervised learning. In Advanced Video and Signal Based Surveillance, 2009. AVSS'09. Sixth IEEE International Conference on, pages 529–534. Ieee, 2009.

50. Rodríguez, T. and García, N.: An adaptive, real-time, traffic monitoring system. Machine Vision and Applications, 21(4):555–576, 2010.

51. Mishra, P. K., Athiq, M., Nandoriya, A., and Chaudhuri, S.: Video-based vehicle detection and classification in heterogeneous traffic conditions using a novel kernel classifier. IETE journal of research, 59(5):541–550, 2013.

52. Cheng, H.-Y. and Hsu, S.-H.: Intelligent highway traffic surveillance with self-diagnosis abilities. IEEE Transactions on Intelligent Transportation Systems, 12(4):1462–1472, 2011.

53. Corral-Soto, E. R. and Elder, J. H.: Slot cars: 3d modelling for improved visual traffic analytics. In The IEEE Conference on Computer Vision and Pattern Recognition (CVPR) Workshops, 2017.

54. Bas, E., Tekalp, A. M., and Salman, F. S.: Automatic vehicle counting from video for traffic flow analysis. In Intelligent Vehicles Symposium, 2007 IEEE, pages 392–397. Ieee, 2007.

55. Nedrich, M. and Davis, J. W.: Detecting behavioral zones in local and global camera views. Machine vision and applications, 24(3):579–605, 2013.

56. Yang, B. and Nevatia, R.: Multi-target tracking by online learning of non-linear motion patterns and robust appearance models. In Computer Vision and Pattern Recognition (CVPR), 2012 IEEE Conference on, pages 1918–1925. IEEE, 2012.

57. Hospedales, T., Gong, S., and Xiang, T.: A markov clustering topic model for mining behaviour in video. In Computer Vision, 2009 IEEE 12th International Conference on, pages 1165–1172. IEEE, 2009.

58. Liao, W., Rosenhahn, B., and Yang, M.: Video event recognition by combining hdp and gaussian process. In Proceedings of the IEEE International Conference on Computer Vision Workshops, pages 19–27, 2015.

59. Zhao, X., Gong, D., and Medioni, G.: Tracking using motion patterns for very crowded scenes. In Comp.Vis.–ECCV 2012, pages 315–328. Springer, 2012.

60. Kratz, L. and Nishino, K.: Tracking with local spatio-temporal motion patterns in extremely crowded scenes. 2010.

61. Song, X., Shao, X., Zhao, H., Cui, J., Shibasaki, R., and Zha, H.: An online approach: Learning-semantic-scene-by-tracking and tracking-by-learning-semantic-scene. In Computer Vision and Pattern Recognition (CVPR), 2010 IEEE Conference on, pages 739–746. IEEE, 2010.

62. Manen, S., Kwon, J., Guillaumin, M., and Van Gool, L.: Appearances can be deceiving: Learning visual tracking from few trajectory annotations. In European Conf. on Comp.Vis., pages 157–172. Springer, 2014.

63. Rasmussen, C. E.: Gaussian processes in machine learning. In Summer School on Machine Learning, pages 63–71. Springer, 2003.

64. Julier, S. J. and Uhlmann, J. K.: New extension of the kalman filter to nonlinear systems. In Signal processing, sensor fusion, and target recognition VI, volume 3068, pages 182–194. International Society for Optics and Photonics, 1997.

65. Wan, E. A. and Van Der Merwe, R.: The unscented kalman filter for nonlinear estimation. In Proceedings of the IEEE 2000 Adaptive Systems for Signal Processing, Communications, and Control Symposium (Cat. No. 00EX373), pages 153–158. Ieee, 2000.

66. Kristan, M., Leonardis, A., Matas, J., Felsberg, M., Pflugfelder, R., Cehovin Zajc, L., Vojir, T., Hager, G., Lukezic, A., Eldesokey, A., et al.: The visual object tracking vot2017 challenge results. In Proceedings of the IEEE International Conference on Computer Vision, pages 1949–1972, 2017.

67. Milan, A., Leal-Taixé, L., Reid, I., Roth, S., and Schindler, K.: Mot16: A benchmark for multi-object tracking. arXiv preprint arXiv:1603.00831, 2016.

68. Sivaraman, S. and Trivedi, M. M.: A general active-learning framework for on-road vehicle recognition and tracking. IEEE Transactions on Intelligent Transportation Systems, 11:267–276, 2010.

69. Vondrick, C., Patterson, D., and Ramanan, D.: Efficiently scaling up crowdsourced video annotation. Int. J. of Comp.Vis., pages 1–21, 2013.

70. Roess, R. P., Prassas, E. S., and McShane, W. R.: Traffic engineering. Pearson/Prentice Hall, 2004.

VITA

NAME	Yanzi Jin
EDUCATION	B.A., Software Engineering, Dalian University of Technology, Dalian, Liaoning, China, 2008
	Ph.D. Computer Science, University of Illinois at Chicago, Chicago, IL, 2019
TEACHING	Program Design (CS111, Fall 2012)
	Intro to Networking (CS450, Spring 2013).
PUBLICATIONS	Jin, Y. and Eriksson, J.: Fully automatic, real-time vehicle tracking for surveillance video. Computer and Robotic Vision, 2017.